A Four-Hierarchy method for the design of organic Rankine cycle (ORC) power plants

Guopeng Yu[1], Qinggang Wang[2,#], Zhibin Yu[3], Na Zhang[2,*], Pingjian Ming[1]

1. Sino-French Institute of Nuclear Engineering and Technology, Sun Yat-sen University, Zhuhai, China

2. School of Civil Engineering and Architecture, East China Jiaotong University, Nanchang, China

3. James Watt School of Engineering, University of Glasgow, United Kingdom, G12 8QQ

[*]Corresponding author: zhangna881127@163.com

[#]Co-first author who contributed equally.

Abstract

In this paper, a practical and general-adapted optimization and decision-making method is proposed for thermal systems designed for a wide range of energy field regarding organic Rankine cycle and thermodynamic cycles. This method is composed of four progressive hierarchies including modelling, optimization, scheme comparison and decision-making. To demonstrate the Four-Hierarchy method, performance of a basic trans-critical ORC and a recuperative trans-critical ORC are analyzed and compared. The NSGA-II algorithm is adopted to obtain the Pareto optimal frontier. Four decision-making methods which are Shannon Entropy, modified LINMAP, TOPSIS and TLFDM are applied for evaluating the Pareto set points. Furthermore, the final Pareto-optimal solution is determined by the root-mean-square difference, correlation coefficient and standard deviation in the Taylor diagram. The optimal results indicate that the final Pareto-optimal solution often appears at LINMAP and TLFDM points. In contrast with basic trans-critical ORC, the recuperative trans-critical ORC can always improve the system's thermodynamic performance. But the techno-economics is only enhanced when the energy grade of heat source is sufficient. The most beneficial improvement is the average reduction of heat transfer area per net output power by more than 27.0% and 30.0% in the medium temperature and high temperature geothermal reservoirs, respectively. Based on the case study, the presented method has proved its application value, and has shown its promising applicability in a wide range of energy field regarding organic Rankine cycle and thermodynamic cycles for energy conversion.

Keywords: Four-Hierarchy design method; Trans-critical organic Rankine cycle; Multi-objective optimization; Three-level fuzzy decision; Taylor diagram

1 Introduction

Rapid economic and social development with the intensification of human activities has increased the consumption of fossil fuels, leading to a huge demand for the energy supply. Effective utilization of sustainable resource like geothermal energy has drawn much attention in recent years, which offers the wild availability, large capacity, and stability. Innovative optimization algorithms and decision-making methods are emerging for improving the system's performance. Concerning the utilization of different heat sources, the organic Rankine cycle (ORC) has been currently regarded as the preferred solution for power generation from low grade heat sources [1-7]. Accordingly, particular attention is paid to develop a general methodology for integrating modelling, optimizing and decision-making process of ORC system in the present work.

Summarizing from the previous studies, a large amount of literature has focused on the stochastic algorithm and optimization design to enhance the performance of geothermal ORC systems. Cetin et al. [8] applied the exergy analysis, Simulated Annealing algorithm, and Gravitational Search algorithm for the thermodynamic performance optimization of a binary geothermal power plant. The optimal results showed that the exergy efficiency obtained by the three methods were 14.48%, 30.62% and 38.49%, respectively. Kolahi et al. [9] investigated a binary flash geothermal ORC system integrated desalination system by utilizing Particle Swarm algorithm. The single objective optimization results revealed that fresh water flow rate of the paralleled system was higher than the series system. Pratama et al. [10] developed a robust design optimization methodology in contrast with the standard design to ensure the stable operation of geothermal ORC system. The Pareto optimal frontier discovered the expected power production increased by 1.5% and the heat transfer area of heat exchangers decreased by 34%. Erdeweghe et al. [11] constructed a two-step optimization method accounting for the off-design behavior which firstly acquired the maximum net present value and then the highest net output power. The off-design results demonstrated that the net output power increased by 1.95~4.75MW while the environment temperature decreased from 29.07 to -4.08℃. Karimi et al. [12] studied the basic, recuperative and two-stage geothermal ORC systems from the thermodynamic, economic and exergoeconomic perspectives. The linear optimization method illustrated that superheat degree and working fluids exerted considerable influence on the whole system performance. Liu et al. [13] proposed a weighted summation method programmed by using Microsoft Excel, which integrated the thermal efficiency, exergy efficiency, net output power and system capitalized cost as one objective function to search the optimal ORC layouts. The evaluation results showed that the basic ORC with R123 was the most appropriate for 80~90℃ geothermal sources. Arslan et al. [14] employed the artificial neural network integrated with a back-propagation learning algorithm to evaluate the economic performance of a binary trans-critical geothermal ORC plant. The life cycle cost decision-making method was used to determine the best system design. The optimal results explained that the maximum benefit was 124.88 million dollars when the installed capacity was 64.2MW.

To exploit possible utilization of geothermal sources, the multi-generation system comprising of cooling, heating, and electricity production, as well as other newly combined ORC have been presented to maximize the energy and exergy efficiency. Alimont et al. [15] explored five applications of geothermal sources including district heating, adsorption cooling, ORC power production, thermal cascade system and combined heat and power configurations. When the temperature was below 300℃, the optimized exergy efficiency of district heating reached 40~50%, and the favorable utilization was the combined heat and power configuration when exceeding 300℃. Cao et al. [16] carried out thermodynamic and thermo-economic performance evaluation for a geothermal poly-generation plant. The parametric study exhibited that the net output power and heating load increased by 16.4% and 14.9% along with the cooling capacity and hydrogen production decreased by 38.9% and 18.5%. Musharavati et al. [17] evaluated the thermodynamic and exergoeconomic performance of an integrated geothermal system. The binary objective optimization results found out that the Pareto-optimal solution with exergy efficiency and electrical cost rate were 22.11% and 12.52$/h. Aliahmadi et al. [18] proposed a novel geothermal ORC-TEG system to recover heat from reinjected well. The investigation revealed that regenerative ORC held the maximum exergy efficiency, and the TEG configuration produced the maximum output power. Lu et al. [19] put forward a composition-adjustable zeotropic ORC system to solve the off-design problem. The optimal results explained that the annual average net output power and thermal efficiency increased by 0.52% and 2.2%, with a decrease of 21.43% in electricity cost.

During the optimization procedures, it may occur that one objective is satisfied while the other has to deviate from its ideal value. On this occasion, the evolutionary optimization methodologies including genetic algorithm and non-dominated sorting genetic algorithm-II (NSGA-II) have been successfully applied to search for compromising solutions to meet decision-maker requirements. Nasruddin et al. [20] compared ORC and Kalina cycles performance in terms of exergy, exergoeconomic and exergoenvironmental analysis in a binary geothermal power plant. It was concluded that ORC was more suitable for acquiring the highest exergy efficiency, per unit power generation and total environmental impact. Pratama et al. [10] quantified the energy loss and pressure reduction for the binary-flash geothermal cycle using the genetic algorithm to optimize net present value and output power. The results demonstrated that R601a resulted in maximum net present value of 2.92million dollars and highest output power with 27.88MW. Additionally, the pressure drop and energy destruction were 0.37~0.93bar and 0.53MW. Wang et al. [21] employed NSGA-II to optimize the thermodynamic and economic performance of a binary flash cycle. TOPSIS decision-making method was adopted to find the Pareto-optimal solution. The weighting factor was studied to reveal the effect on the objective function and decision variable, which was recommended within the range of 0.1~0.6. Imran et al. [22] dealt with the hydraulic and thermal models of evaporator for low temperature geothermal ORC system with NSGA-II algorithm. The primary geometrical parameters were length, width and plate spacing. The optimal results showed that allowable pressure and evaporator cost were 30~40kPa and 3000~3500$.

The determination of objective functions is relevant with thermodynamic and techno-economic properties, and the decision variables are initialized with stochastic values for subsequent analysis. Liu et al. [23] analyzed the effect of pinch point temperature difference on system performance. The working fluid mass flow rate, net output power, irreversible loss, total thermal conductance, size parameter and volumetric flow ratio were investigated. The results presented that lower pinch point temperature difference led to higher net output power and investment, with an optimal variation range of 2~21℃. Shokati et al. [24] performed the comparative analysis with basic, dual-pressure, dual-fluid ORCs and Kalina cycle for the medium temperature geothermal power production. The parametric study evaluated the effect of ammonia concentration and operation pressure on system thermodynamic and enhanced exergoeconomic performance. The optimized results demonstrated that the dual-pressure ORC obtained the maximum electricity production and Kalina cycle got the minimum unit cost of power produced. Hettiarachchi et al. [25] provided a cost-effective design method which taken heat transfer area per net output power as the single objective function. The optimized results illustrated that ammonia obtained the minimal objective value but lower cycle efficiency, which was restricted use under the high evaporation pressure for the vapor droplet may fall into the two-phase region after expansion.

The brief literature reviews show that researchers tend to develop multiple and scattered methodologies for the design of ORC power plants. In addition to the reliability and applicability, it may take some time associated with modelling and verification for a variety of heat sources. Furthermore, it is worth noting that the Pareto-optimal solutions judged by numerous decision-making methods vary greatly, making it difficult to accurately determine the optimization results. Therefore, the goal of this work is to present a systematic and generic design method, which integrates the modelling, optimizing, scheme comparing and decision-making steps. It provides a general-adapted approach to get the final Pareto-optimal solution, which can be widely employed in geothermal field, and much wider applications including industrial and engine waste heat recovery, co-generation systems, biomass energy utilization, solar ponds, etc.

In this study, the multi-objective optimization models based on NSGA-II with regard to basic trans-critical and recuperative trans-critical ORC are constructed for further elaborating the Four-Hierarchy method. Six working fluids including R227ea, R134, R143a, R290, R1270 and R142b are selected for the simulated operating conditions of two typical medium (GR-I) and high (GR-II) temperature geothermal reservoirs. The Pareto optimal frontiers are acquired by setting two objectives with net output power and heat transfer area per net output power as well as five decision variables with evaporation pressure, turbine inlet temperature, condenser temperature, evaporator pinch point temperature, and condenser pinch point temperature. Meanwhile, thirteen decision criteria covering environmental, thermodynamic, and techno-economic perspectives are evaluated for the performance analysis. Afterwards, four decision-making methods including Shannon Entropy, modified LINMAP (combined with Relative entropy), modified TOPSIS (integrated with Shannon entropy and Relative entropy), and TLFDM (Three-level fuzzy decision method) are employed to determine Pareto-optimal solutions. Lastly, these four Pareto-optimal solutions are evaluated by Taylor diagram to identify the optimization results.

2 Methodology description

The Four-Hierarchy method can provide a feasible basis for the comprehensive analysis and optimization of ORC system. As depicted in Fig. 1, this approach consists of the modelling, optimization, scheme comparison and decision-making hierarchy, which exhibits a progressive pyramid shape. At first, the evaluation criteria need to be determined according to the specific characteristics of system and the preference of decision-maker. For the geothermal sources exploitation, the environmental, thermodynamic, heat transfer, techno-economic, and equipment reliability models are constructed. Afterwards, by selecting the appropriate objective functions, the optimization is performed to obtain the target performance under different operating conditions. For the single-objective optimization, the decision criteria values are acquired under the same condition while getting the maximum net output power. Furthermore, Three-level fuzzy decision method (TLFDM) which takes into account the effect of the former level on the latter is used for subsequent evaluation of the priority between different schemes. And all the single-objective optimization works have been explicitly illustrated in a previous article [26]. As for the multi-objective optimization, the stochastic algorithm is used to get the Pareto optimal frontier. The Pareto-optimal solutions are assessed by four decision-making methods which are Shannon Entropy, modified TOPSIS, LINMAP and TLFDM. To solve the equivalent distance problem, the traditional Euclidean distance is replaced by Relative entropy. Eventually, the final optimal result is obtained by comparing the four decision-making points in the Taylor diagram.

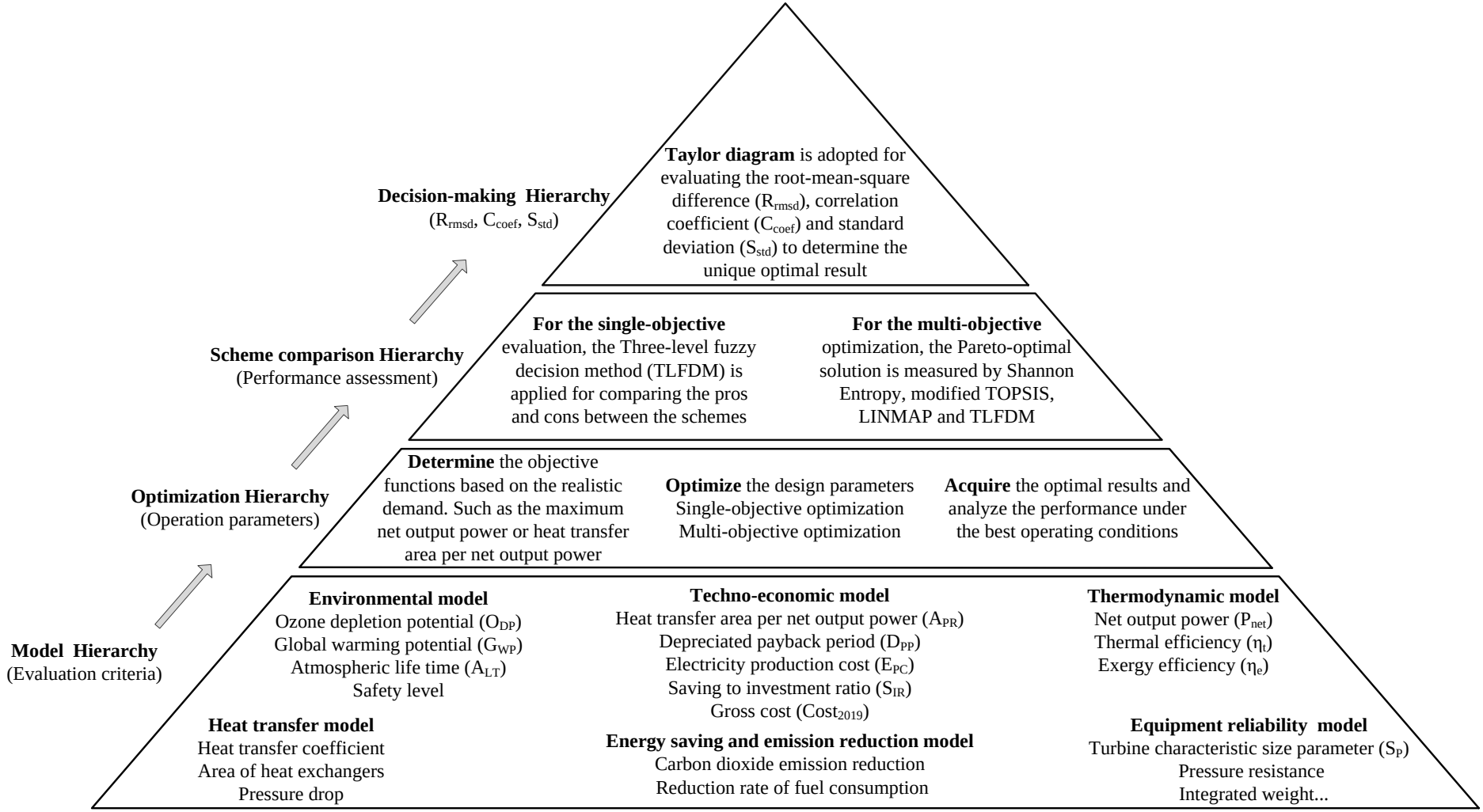

Fig. 1. Description of the Four-Hierarchy method.

2.1 Mathematical modelling

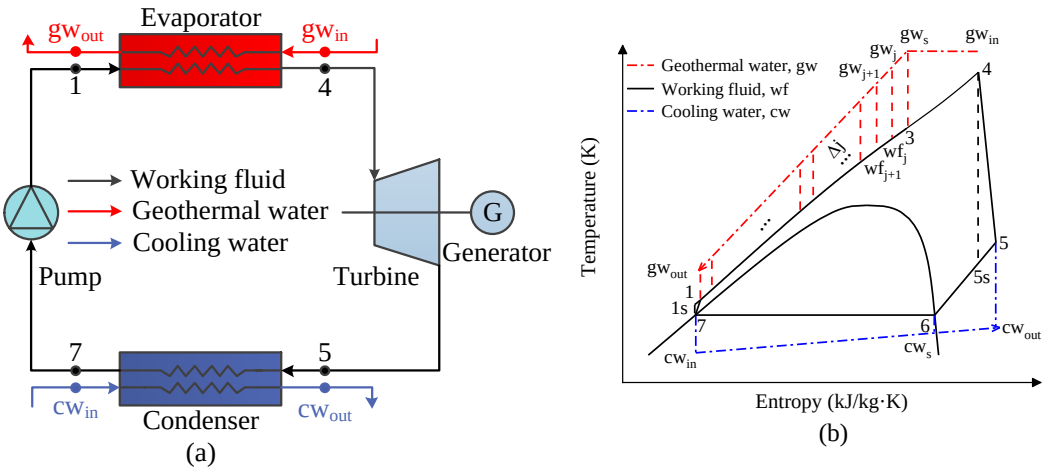

Fig. 2. (a) Schematic diagram and (b) T-s diagram of trans-critical B-ORC system.

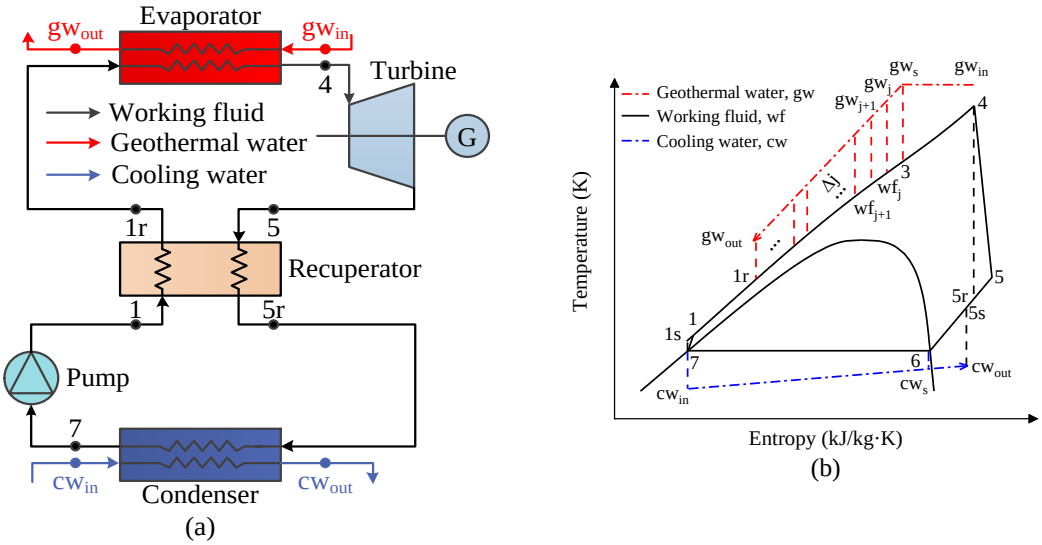

Fig. 3. (a) Schematic diagram and (b) T-s diagram of trans-critical R-ORC system.

In the aspect of the heat source, two geothermal reservoirs referring to medium temperature (GR-I with well-head outlet of 182.23°C) and high temperature (GR-II with well-head outlet of 223.47°C) are investigated. The optimizing models are basic trans-critical ORC (B-ORC) and recuperative trans-critical ORC (R-ORC) systems. As illustrated in Fig. 3, the working fluid is initially pumped to supercritical condition (state point 7 to 1), and then entering the recuperator (state point 1 to 1r) to absorb heat from overheated vapor discharged from the turbine (state point 5 to 5r) before condensation (state point 5r to 7). During the evaporation (state point 1r to 4), the working fluid temperature reaches the maximum while the geothermal water outlet temperature is slightly higher than the B-ORC system. Next, the working fluid flows into the turbine for expansion (state point 4 to 5) to complete the entire cycle.

Furthermore, the selection of six working fluids including R227ea, R134a, R143a, R290, R1270 and R142b not only depends on the thermodynamic properties, suggesting that evaporation pressure (P_4) and turbine inlet temperature (T_4) should exceed critical point but avoid decomposition. Meanwhile, it also needs to take the environmental characteristics like Safety level, atmospheric life time (A_{LT}), ozone depletion potential (O_{DP}) and global warming potential (G_{WP}) into consideration.

Thermodynamic and techno-economic criteria for a comprehensive evaluation of geothermal trans-critical ORC systems, including net output power (P_{net}), thermal efficiency (η_t), exergy efficiency (η_e) as well as heat transfer area per net output power (A_{PR}), turbine characteristic size parameter (S_P), total cost ($Cost_{2019}$), electricity production cost (E_{PC}), depreciated payback period (D_{PP}) and saving to investment ratio (S_{IR}) are demonstrated.

The simulation of two geothermal ORC systems is conducted in the original Matlab code. The following formulas are introduced to describe the thermodynamic characteristics of the R-ORC system.

Compression: state point 7 to 1

$$h_1 = h_7 + \left(h_{1s} - h_7\right)/\eta_{pump} \tag{1}$$

Where h_{1s} is the enthalpy of isentropic compression point and η_{pump} represents the pump isentropic efficiency which is set to be 0.7 [26].

Expansion: state point 4 to 5

$$h_5 = h_4 - \left(h_4 - h_{5s}\right) \times \eta_{turbine} \tag{2}$$

Where h_{5s} indicates the enthalpy of isentropic expansion point and $\eta_{turbine}$ denotes the turbine isentropic efficiency which is set to be 0.75 [26].

Recuperative process: state 1 to 1r and 5 to 5r

$$\varepsilon_{recuperator} = \left(T_5 - T_{5r}\right)/\left(T_5 - T_1\right) \tag{3}$$

$$h_{1r} = h_1 + h_5 - h_{5r} \tag{4}$$

Where $\varepsilon_{recuperator}$ means the recuperator effectiveness and sets as 0.8 [6] and the vapor quality x_5 keeps exceeding 1 by increasing the turbine inlet temperature to avoid the working fluid falling into the two-phase region causing liquid slugging.

The working fluid mass flow rate (m_{wf}) is determined by the pinch point temperature difference method. It compares the error of evaporator pinch point temperature ($T_{pinch-e}$) which is set as 10℃ with the iterative one. The m_{wf} is output until the error meets the accuracy requirement (1%).

Assuming the geothermal water outlet temperature (T_{gwout}) to obtain the enthalpy of the state point (h_{gwout}) and then calculate the initial mass flow rate of working fluid.

$$m_{wf} = m_{gw}\left(h_{gwin} - h_{gwout}\right)/\left(h_4 - h_{1r}\right) \tag{5}$$

Evaporation process from state 1r to 3:

$$h_3 = h_{1r} + m_{gw}\left(h_{gws} - h_{gwout}\right)/m_{wf} \tag{6}$$

Where m_{gw} represents the mass flow rate of geothermal water.

Since the single-phase flow region (state point gw_s to gw_{out}) of geothermal water has been distributed into one hundred segments as shown in Fig. 3. The temperature of each segment $T_{gw}(j)$, the enthalpy of working fluid $h_{wf}(j)$ and the iterative pinch point temperature difference $\Delta T_{pinch-e}(j)$ can be calculated from the beginning of the geothermal water phase transition point T_{gws}.

$$\Delta T_{gw} = \left(T_{gws} - T_{gwout}\right)/100 \tag{7}$$

$$T_{gw}(j+1) = T_{gw}(j) - \Delta T_{gw} \tag{8}$$

$$h_{wf}(j+1) = h_{wf}(j) - c_p(j) m_{gw}\left(T_{gw}(j) - T_{gw}(j+1)\right)/m_{wf} \tag{9}$$

$$\Delta T_{pinch-e}(j) = T_{gw}(j) - T_{wf}(j) \tag{10}$$

Condensation: state 5r to 7

$$T_{cws} = T_6 - T_{pinch-c} \tag{11}$$

$$m_{cw} = m_{wf}\left(h_6 - h_7\right)/\left(h_{cws} - h_{cwin}\right) \tag{12}$$

$$Q_{condenser} = m_{wf}\left(h_{5r} - h_7\right) \tag{13}$$

$$h_{cwout} = Q_{condenser}/m_{cw} + h_{cwin} \tag{14}$$

For the exergy analysis of each state point:

$$E_i = m\left[\left(h_i - h_0\right) - T_0\left(s_i - s_0\right)\right] \tag{15}$$

Description of thermodynamic performance evaluation criteria are tabulated in Table 1.

The net output power of ORC system:

$$P_{net} = P_{turbine} - P_{pump} \tag{16}$$

The thermal efficiency of ORC system:

$$\eta_t = P_{net} / Q_{evaporator} \tag{17}$$

The total exergy destruction of ORC system:

$$I_{ORC} = I_{pump} + I_{recuperator} + I_{evaporator} + I_{turbine} + I_{condenser} + I_{cooling\ water} \tag{18}$$

The exergy destruction of cooling water:

$$I_{cooling\ water} = E_{cwout} - E_{cwin} \tag{19}$$

The exergy efficiency of ORC system；

$$\eta_e = P_{net} / \left(P_{net} + I_{ORC}\right) \tag{20}$$

The plate heat exchanger is chosen subjected to its compact structure and high effectiveness, the geometry and heat transfer correlations are expressed in Table 2. The areas of the heat exchanger can be calculated after acquiring each part heat transfer coefficient.

$$A = Q / U / \Delta T_m \tag{21}$$

$$1/U = 1/\alpha_{hot-side} + t/\lambda_{PHE} + 1/\alpha_{cold-side} \tag{22}$$

The techno-economic criteria which cover the system compactness, investments and profit are depicted in Table 3. And the detailed operating parameters and assumptions have been described in a previous study [26].

Table 1 Energy and exergy analysis of main component in R-ORC system.

Component	Energy analysis	Exergy destruction	Exergy efficiency
Pump	$P_{pump} = m_{wf}\left(h_1 - h_7\right)$	$I_{pump} = E_7 - E_1 + P_{pump}$	$\eta_{e-pump} = \left(E_1 - E_7\right)/P_{pump}$
Recuperator	$Q_{recuperator} = m_{wf}\left(h_{1r} - h_1\right)$	$I_{recuperator} = E_1 - E_{1r} + E_5 - E_{5r}$	$\eta_{e-recuperator} = \left(E_{1r} - E_1\right)/\left(E_5 - E_{5r}\right)$
Evaporator	$Q_{evaporator} = m_{wf}\left(h_4 - h_{1r}\right)$	$I_{evaporator} = E_{gwin} - E_{gwout} + E_{1r} - E_4$	$\eta_{e-evaporator} = \left(E_4 - E_{1r}\right)/\left(E_{gwin} - E_{gwout}\right)$
Turbine	$P_{turbine} = m_{wf}\left(h_4 - h_5\right)$	$I_{turbine} = E_4 - E_5 - P_{turbine}$	$\eta_{e-turbine} = P_{turbine}/\left(E_4 - E_5\right)$
Condenser	$Q_{condenser} = m_{wf}\left(h_{5r} - h_7\right)$	$I_{condenser} = E_{5r} - E_7 + E_{cwin} - E_{cwout}$	$\eta_{e-condenser} = \left(E_{cwout} - E_{cwin}\right)/\left(E_{5r} - E_7\right)$

Table 2 Plate heat exchanger geometry and heat transfer correlations.

Parameter [27]	Value	Working fluid side	Correlations
Chevron angle, β (°)	60	Single-phase flow of geothermal water	Leveque correlation [28]
Plate width, L_w (m)	0.65	Two-phase flow of geothermal water	Wang and Zhao correlation [29]
Plate thickness, t (m)	0.0005	Supercritical working fluids	Jackson correlation [30]
Corrugation pitch, Λ (m)	0.0085	Cooling part of working fluids	Chisholm correlation [31]
Corrugation depth, b (m)	0.0025	Condensing part of working fluids	Kandlikar correlation [32]
Surface enlargement factor, Φ	1.19	Supercritical working fluids in recuperator	Jackson correlation [30]
Hydraulic diameter, D_h (m)	0.0042	Overheated working fluids in recuperator	Chisholm correlation [31]
Equivalent diameter, D_{eq} (m)	0.005		
Coefficient of thermal conductivity, λ_{PHE} (kW/(m·K))	0.0163		

Table 3 Techno-economic evaluation criteria expression in R-ORC system [26].

Techno-economic criteria	Formula
Heat transfer area per net output power (A_{PR})	$A_{PR} = \left(A_{evaporator} + A_{condenser} + A_{recuperator}\right) / P_{net}$
Turbine characteristic size parameter (S_P)	$S_P = \sqrt{V_5} / \Delta h_{isen}^{0.25}$
Total cost ($Cost_{2019}$) refers to "Bare Module Cost Technique"	$\mathrm{Cos}\,t_{2001} = \mathrm{C}_{BM,\,pump} + \mathrm{C}_{BM,\,evaporator} + \mathrm{C}_{BM,\,turbine} + \mathrm{C}_{BM,\,condenser} + \mathrm{C}_{BM,\,recuperator}$ $\mathrm{Cos}\,t_{2019} = CEPCI_{2019} / CEPCI_{2001}\,\mathrm{Cos}\,t_{2001}$
Electricity production cost (E_{PC})	$E_{PC} = \left(\mathrm{Cos}\,t_{2019} C_{RF} + f_k\,\mathrm{Cos}\,t_{2019}\right) / \left(P_{net} h_{working\ time}\right)$ $C_{RF} = i(1+i)^{time} / \left((1+i)^{time} - 1\right)$
Depreciated payback period (D_{PP})	$D_{PP} = -\ln\left(1 - k\,\mathrm{Cos}\,t_{2019} / F_{n0}\right) / \ln(1+k)$ $F_{n0} = E_P\left(P_{net} h_{working-time}\right) - f_k\,\mathrm{Cos}\,t_{2019}$
Saving to investment ratio (S_{IR})	$S_{IR} = B_{time} / C_{time}$ $B_{time} = \sum_{j=1}^{time}\left(P_{net} h_{working-time} E_p (1+r)^j / (1+i)^j\right)$ $C_{time} = \sum_{j=0}^{time}\left(\left(f_k\,\mathrm{Cos}\,t_{2019}\right)(1+r)^j / (1+i)^j\right)$

2.2 Model validation

The constructed B-ORC and R-ORC models are validated with the data reported in the published papers [6, 33]. As summarized in Table 4, the maximum error between yielded thermal efficiency in B-ORC system with the reference data is 1.23%. And it can be noticed from Fig. 4 that the variations of plant efficiency and thermal efficiency with turbine inlet temperature and geothermal water inlet temperature present good agreement, which indicates that the simulated results are reliable for the following analysis.

Table 4 Validation of the constructed B-ORC model.

Output parameter	Reference	Calculated	Error (%)
Heat source (water) outlet temperature, T_{hso} (℃)	70.3	70.9773	0.9542
Cooling medium (water) outlet temperature, T_{cmo} (℃)	17.2	17.2328	0.1903
Working fluid (R134a) mass flow rate, m_{wf} (kg/s)	0.1402	0.1407	0.3554
Cooling medium mass flow rate, m_{cm} (kg/s)	3.0990	3.0628	1.1681
Turbine outlet vapor quality, x_5 (kg/kg)	1.12	1.1201	0.0089
Net output power, P_{net} (kW)	4.7	4.7436	0.9191
Thermal efficiency, η_t (%)	14.0	14.1748	1.2332

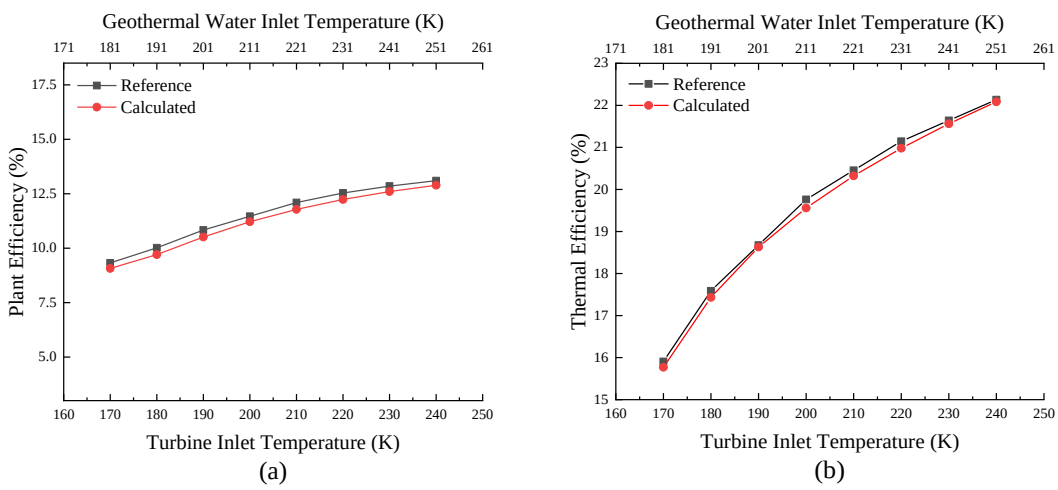

Fig. 4. Validation of the constructed R-ORC model.

3 Multi-objective optimization

The NSGA-II (Non-dominated sorting genetic algorithm-II) method is adopted to conduct the two contradictory objectives optimization and get the Pareto optimal frontier. The binary objectives selected are P_{net} and A_{PR} which reflect the thermodynamic and techno-economic performance. The heat exchanger areas will increase which leads to an increment of A_{PR} when pursuing higher P_{net}. Higher A_{PR} indicates more expensive system cost. Therefore, it is necessary to find a compromising solution to acquire relatively higher P_{net} and lower A_{PR}. Five decision variables including evaporation pressure (P_4), turbine inlet temperature (T_4), condensing temperature (T_{cond}), evaporator pinch point temperature ($T_{pinch\text{-}e}$), and condenser pinch point temperature ($T_{pinch\text{-}c}$) are defined.

Table 5 Input parameters of NSGA-II.

Parameter	Value
Population size	100
Maximum generation	120
Crossover fraction	0.8
Mutation rate	0.2
Selection function	Tournament
Tournament size	2
Objective functions	P_{net}(max), A_{PR}(min)
Decision variables	P_4, T_4, T_{cond} (305~313K), $T_{pinch\text{-}e}$ (3~10K), $T_{pinch\text{-}c}$ (3~10K)
Decision methods	Shannon Entropy, Relative Entropy & Shannon Entropy & TOPSIS, Relative Entropy & LINMPA, Three-level fuzzy decision method

As shown in Fig. 5, the core principle of NSGA-II lies in the five decision variables are obtained randomly within the iteration range to calculate thermodynamic and techno-economic criteria values. Subsequently, the rank and crowding distance of each individual are assigned by the relative magnitude of P_{net} and A_{PR}. The individual selected into the mating pool firstly depends on the lower rank and then higher crowding distance. It compares crowding distance when rank is equal. Afterwards, the crossover and mutation are operated to produce offspring. And the lower ranking individuals are eliminated to remain the constant population size. As observed in Table 5, four decision methods are summarized for further determining the Pareto-optimal solutions.

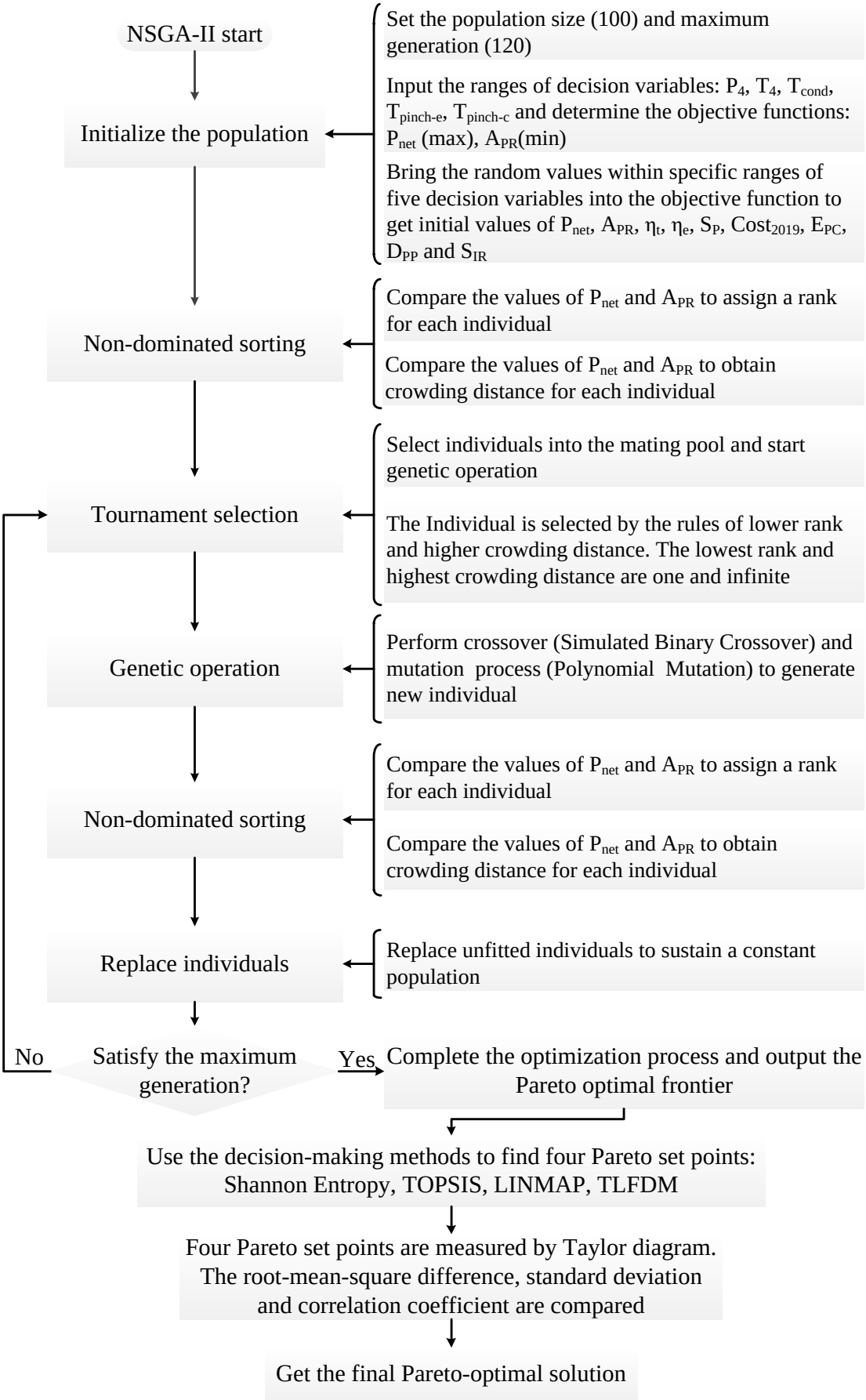

Fig. 5. Flow chart of NSGA-II optimization, decision-making and evaluation procedures.

4 Decision-making and evaluation methods

After NSGA-II optimization, the optimizing results are elucidated from the Pareto optimal frontier. It can be concluded from the previous studies [34-38] that the Pareto set points obtained by different decision-making methods vary greatly, making it difficult for the decision-maker to judge which method is better. In this literature, several decision-making methods including Shannon Entropy, modified TOPSIS, LINMAP and TLFDM are adopted to determine four Pareto-optimal solutions. In order to get the unique Pareto-optimal result, the Taylor diagram can be utilized as an effective technique to evaluate the priority between these decision-making points.

4.1 Shannon Entropy decision-making

Shannon Entropy is normally regarded as the weighting assignment method according to the uncertainty discrepancy of information.

The first step is to normalize the scheme matrix.

$$P_{ij} = p_{ij} \Big/ \sum_{i=1}^{n} p_{ij} \tag{23}$$

Where p_{ij} is the objective value, while $i = 1...n$ and $j = 1...m$ represent the quantities of scheme and objective function.

The information entropy index is expressed as bellows:

$$h_j = -\frac{1}{\ln(n)} \sum_{i=1}^{n} P_{ij} \ln\left(P_{ij}\right) \tag{24}$$

The weighting matrix is given as:

$$w_j = \left(1 - h_j\right) \Big/ \sum_{j=1}^{m} \left(1 - h_j\right) \tag{25}$$

Shannon Entropy point is searched from the Pareto optimal frontier which ranked first.

$$W_i = P_{ij} \cdot w_j \tag{26}$$

Where W_i is the scheme matrix that sorts in descending order after decision-making.

4.2 Modified TOPSIS and LINMAP decision-making

Conventional TOPSIS (Technique for Order Preference by Similarity to Ideal Situation) point is identified by the shortest Euclidean distance between Pareto-optimal solution with the ideal point as well as the longest distance with nadir point. As depicted in Fig. 6, it may occur that P_1 and P_2 get the equivalent distances, which cannot distinguish the pros and cons of the two Pareto set points. Therefore, the relative entropy initially used to estimate the difference between probability distribution is introduced as a substitute.

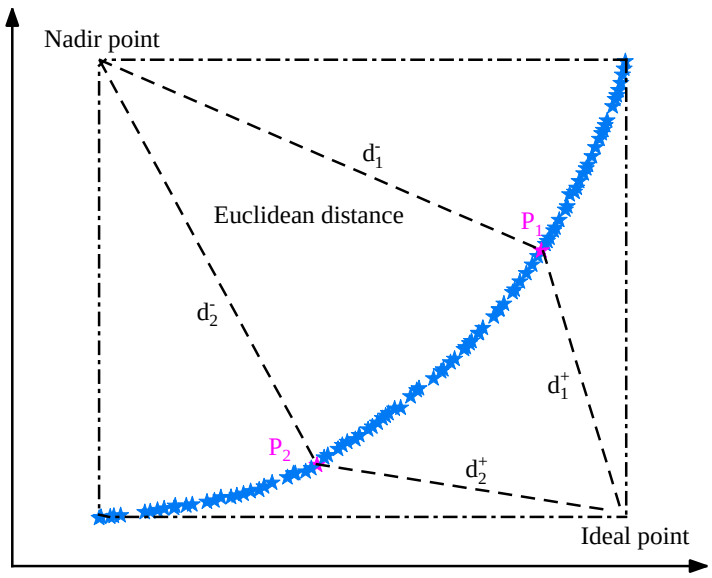

Fig. 6. Conventional TOPSIS point determined by Euclidean distance.

Normalization of the scheme matrix:

$$Q_{ij} = q_{ij} \Big/ \sqrt{\sum_{i=1}^{n} q_{ij}^{2}} \tag{27}$$

The weighting matrix R_i is shown as:

$$R_i = Q_{ij} \cdot w_j \tag{28}$$

The objective weighting w_j is derived from Shannon Entropy.

Positive $Z^+ = \left(z_1^+, z_2^+, ..., z_n^+\right)$ and negative $Z^- = \left(z_1^-, z_2^-, ..., z_n^-\right)$ ideal solutions are explained as below:

$$z_j^+ = \max_{1 \le i \le n} \left\{R_{ij}\right\} \quad \text{for the higher the better criteria} \tag{29}$$

$$z_j^- = \min_{1 \le i \le n} \left\{R_{ij}\right\} \quad \text{for the higher the better criteria} \tag{30}$$

$$z_j^+ = \min_{1 \le i \le n} \{R_{ij}\} \quad \text{for the lower the better criteria} \tag{31}$$

$$z_j^- = \max_{1 \le i \le n} \{R_{ij}\} \quad \text{for the lower the better criteria} \tag{32}$$

Relative entropy distance is calculated as:

$$d_i^+ = \sum_{j=1}^{m} \left\{ z_j^+ \lg \frac{z_j^+}{R_i} + \left(1 - z_j^+\right) \lg \frac{1 - z_j^+}{1 - R_i} \right\} \tag{33}$$

$$d_i^- = \sum_{j=1}^{m} \left\{ z_j^- \lg \frac{z_j^-}{R_i} + \left(1 - z_j^-\right) \lg \frac{1 - z_j^-}{1 - R_i} \right\} \tag{34}$$

The modified TOPSIS point is selected according to the maximum coefficient S_i:

$$S_i = \frac{d_i^-}{d_i^- + d_i^+} \tag{35}$$

Based on the relative entropy, the modified LINMAP (Linear Programming Technique for Multidimensional Analysis of Preference) point is defined by the smallest d_i^+.

4.3 TLFDM decision-making

Three-level fuzzy decision method (TLFDM) [26] covers thirteen evaluation criteria involving the environmental, thermodynamic and techno-economic indexes. Numerical data are output during the execution of the optimization process. For the evaluation criteria of P_{net}, η_t, η_e and S_{IR}, the higher value represents the better performance. On the contrary, lower-the-better criteria are the Safety level, A_{LT}, O_{DP}, G_{WP}, A_{PR}, S_P, $Cost_{2019}$, E_{PC} and D_{PP}.

Furthermore, the subjective importance ranks within the same hierarchy are given as:

First level: O_{DP}>G_{WP}>A_{LT}>Safety level.

Second level: η_e>η_t>P_{net}.

Third level: E_{PC}>S_{IR}>D_{PP}>$Cost_{2019}$>A_{PR}>S_P.

Two pair-wise comparison matrices are constructed for schemes and levels and the decision-making results can be acquired by the following formula:

$$\boldsymbol{B_i} = \boldsymbol{W_i} \times \boldsymbol{R_i} \tag{36}$$

Where $\boldsymbol{R_i}$ and $\boldsymbol{W_i}$ represent the weighting matrices for schemes and levels.

4.4 Taylor diagram evaluation

Taylor diagram [39] is capable of graphically evaluating the simulation capability of multiple complex models based on root-mean-square difference (R_{rmsd}), correlation coefficient (C_{coef}), and standard deviation (S_{std}). These three criteria represent the discrepancy, similarity, and variation amplitude between simulated and ideal results.

The formulas are expressed as:

$$R_{rmsd} = \sqrt{\frac{1}{n}\sum_{i=1}^{n}\left[\left(f_i - \overline{f}\right) - \left(r_i - \overline{r}\right)\right]^2} \tag{37}$$

$$C_{coef} = \frac{\sum_{i=1}^{n}\left(f_i - \overline{f}\right)\left(r_i - \overline{r}\right)}{\sqrt{\sum_{i=1}^{n}\left(f_i - \overline{f}\right)^2}\sqrt{\sum_{i=1}^{n}\left(r_i - \overline{r}\right)^2}} \tag{38}$$

$$S_{std_f} = \sqrt{\frac{1}{n}\sum_{i=1}^{n}\left(f_i - \overline{f}\right)^2}, S_{std_r} = \sqrt{\frac{1}{n}\sum_{i=1}^{n}\left(r_i - \overline{r}\right)^2} \tag{39}$$

Where f implies the normalized matrix, including thermodynamic and techno-economic criteria values for Shannon Entropy, TOPSIS, LINMAP and TLFDM points, r indicates the reference (ideal point) data, $\overline{f}$ and $\overline{r}$ are their corresponding average values, $i = 1...n$ represents criteria number.

5 Results and discussion

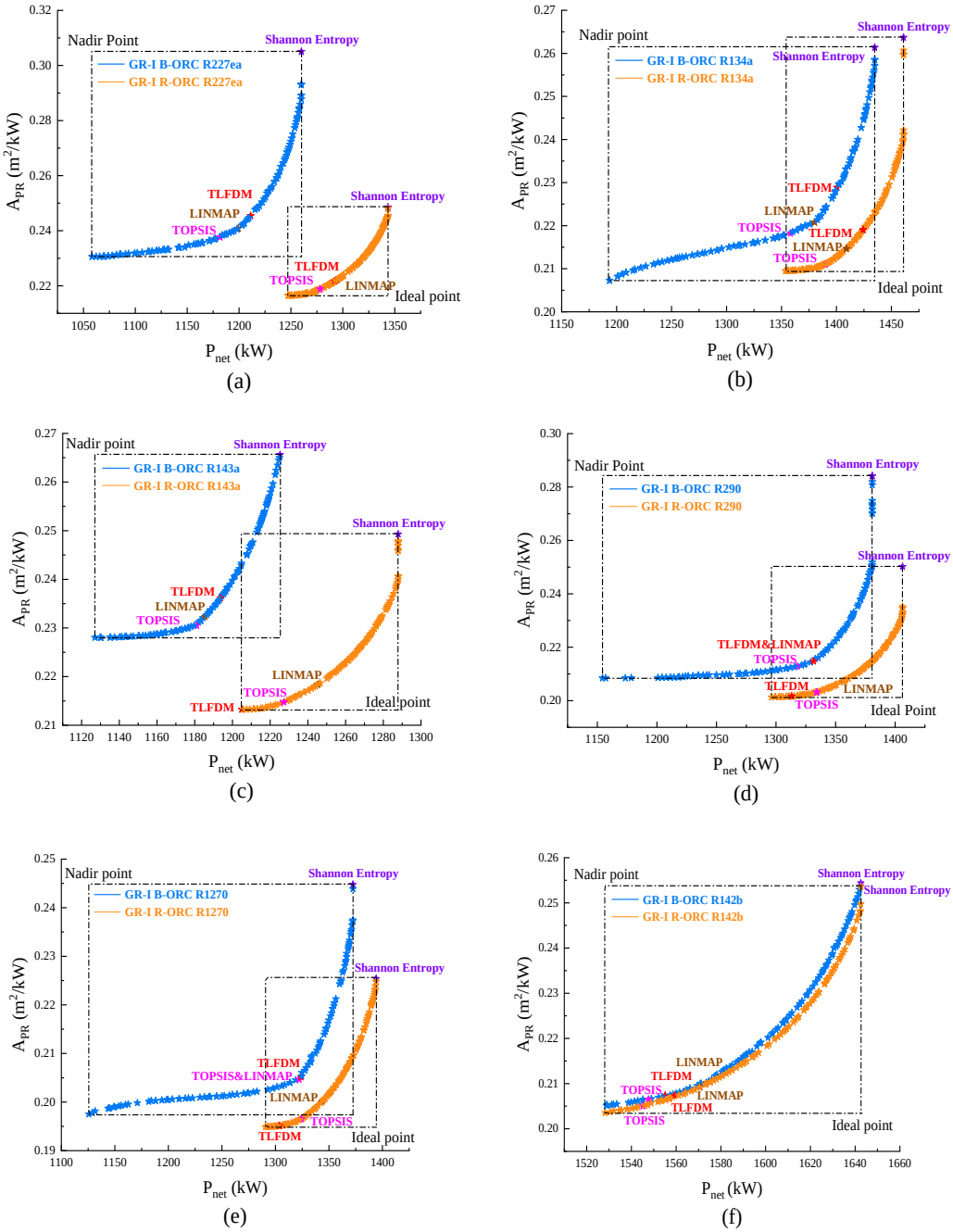

Fig. 7. Pareto optimal frontier and four decision-making points in GR-I.

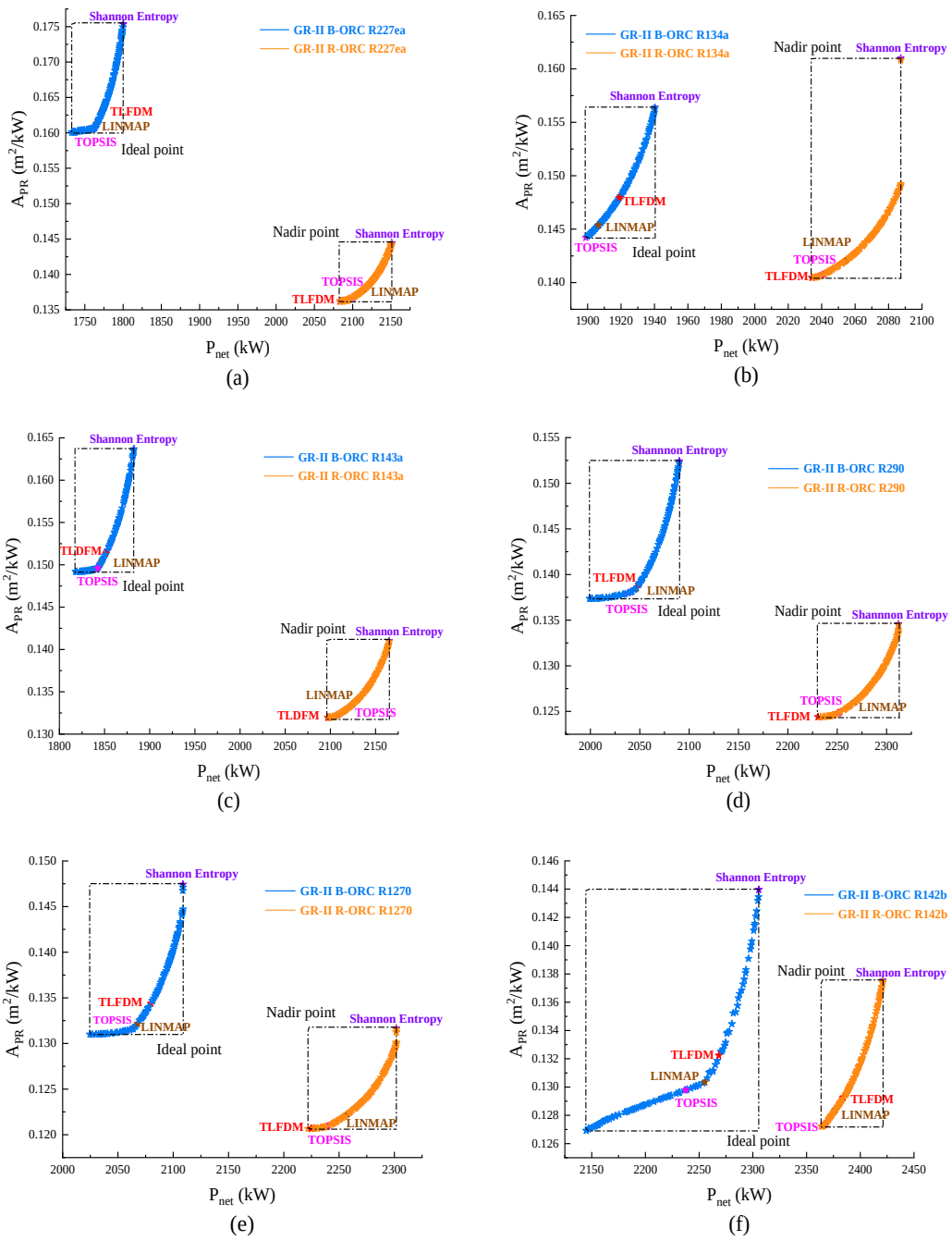

Fig. 8. Pareto optimal frontier and four decision-making points in GR-II.

Figs. 7 and 8 depict the Pareto optimal frontier of NSGA-II optimization for basic trans-critical ORC (B-ORC) and recuperative ORC (R-ORC) systems in medium (GR-I) and high temperature geothermal reservoirs (GR-II). The binary objectives are the maximum net output power (P_{net}) and minimum heat transfer area per net output power (A_{PR}). It is observed that A_{PR} increases moderately first and then goes up rapidly with an increment of P_{net}, since the total area of heat exchangers increase faster than the P_{net} under higher evaporation pressure and turbine inlet temperature.

Similar phenomena have been observed in previous studies [34, 40], indicating that higher thermodynamic performance leads to a decrease in techno-economic performance. The ideal point occurs at the lower right corner outside the frontier in the rectangle, which represents the theoretical goal to obtain the maximal P_{net} and minimal A_{PR} simultaneously. On the contrary, the nadir point signifies the non-ideal working condition with minimal P_{net} and maximal A_{PR}. In order to ascertain the Pareto-optimal solutions, four decision methods including Shannon Entropy, modified TOPSIS, LINMAP and TLFDM (Three-level fuzzy decision method) are applied, and eventually compared on Taylor diagram. The former three have been commonly used in the decision-making process [34], which only need the optimal results of the objective functions. But TLFDM requires more information about the environmental, thermodynamic and techno-economic properties of the system, which can provide a relatively comprehensive perspective for the decision-maker [26]. Additionally, with restrictions of the schemes (no more than twenty-one) in the three-level performance evaluation [41], the population is divided into small groups with six or seven individuals, and the best individual in each group can enter the next round until the target Pareto-optimal solution is found. Later, the Taylor diagram is used for determining the final Pareto-optimal solution from these four decision-making points by measuring the root-mean-square difference, correlation coefficient and standard deviation [39].

As illustrated in Figs. 7 and 8, it can be observed that R-ORC obtains lower A_{PR} and higher P_{net} compared to the B-ORC system. The mass flow rate of working fluid has increased in R-ORC system, resulting in an increment of P_{net} and total area of heat exchangers, but the increase of P_{net} is more markedly than that of total area of heat exchangers, which verifies that R-ORC may improve the system's thermodynamic performance [6]. The two Pareto optimal frontiers have similar variation range in GR-I while are far apart in GR-II, suggesting that higher temperature working condition is favorable for the optimizing process. Concerning the decision-making points, the Shannon Entropy point is consistent with the maximal P_{net} point at the top of the frontier and the LINMAP point is at the middle. As for the TOPSIS and TLDFM points, they are close to the minimal A_{PR} point in GR-I and GR-II, respectively.

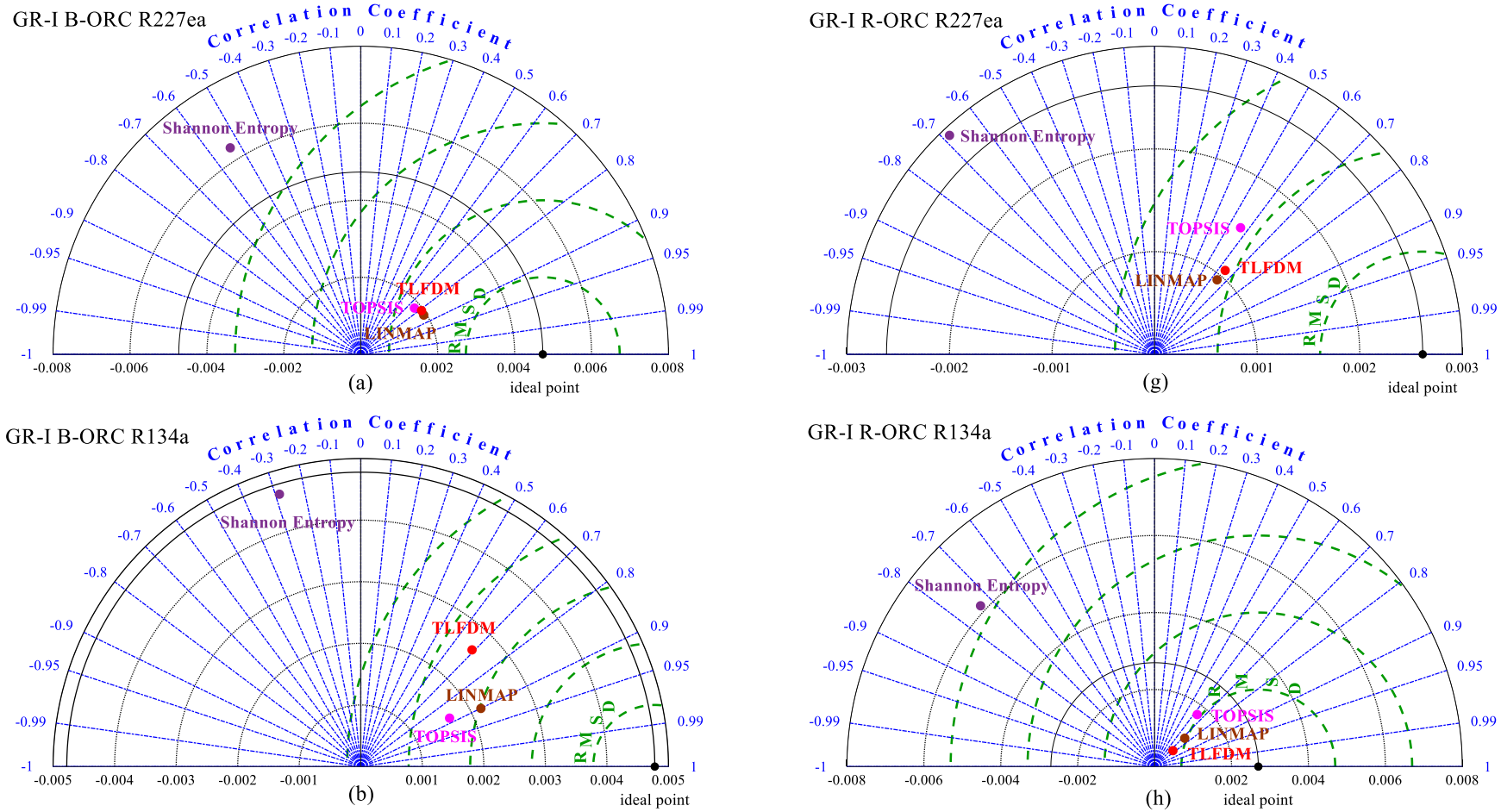
GR-I B-ORC R227ea
Correlation Coefficient
Shannon Entropy
TLFDM
TOPSIS
LINMAP
RMSD
ideal point
(a)
GR-I R-ORC R227ea
Correlation Coefficient
Shannon Entropy
TOPSIS
LINMAP
TLFDM
RMSD
ideal point
(g)
GR-I B-ORC R134a
Correlation Coefficient
Shannon Entropy
TLFDM
LINMAP
TOPSIS
RMSD
ideal point
(b)
GR-I R-ORC R134a
Correlation Coefficient
Shannon Entropy
TOPSIS
LINMAP
TLFDM
RMSD
ideal point
(h)

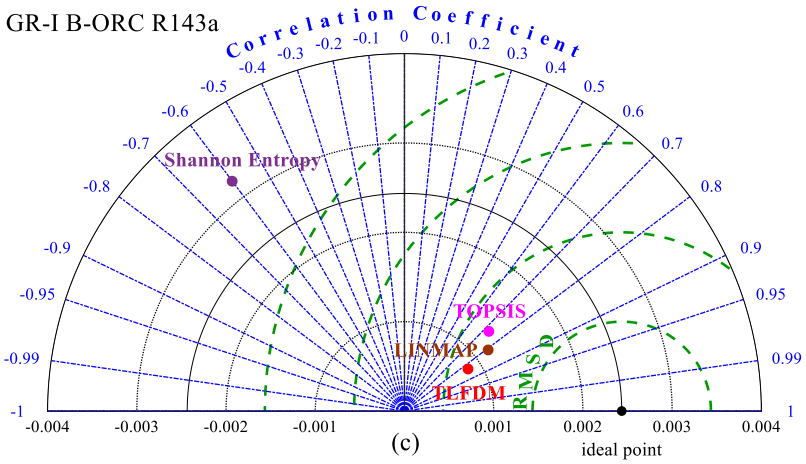
GR-I B-ORC R143a
Correlation Coefficient
Shannon Entropy
TOPSIS
LINMAP
TLFDM
RMSD
ideal point
(c)

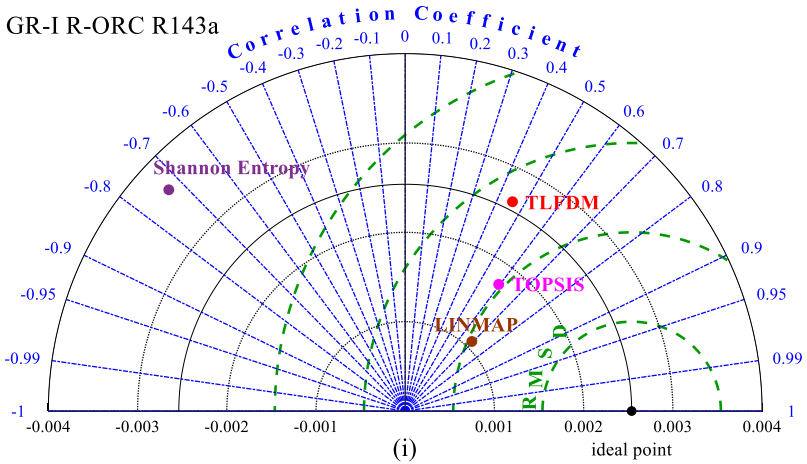
GR-I R-ORC R143a
Correlation Coefficient
Shannon Entropy
TLFDM
TOPSIS
LINMAP
RMSD
ideal point
(i)

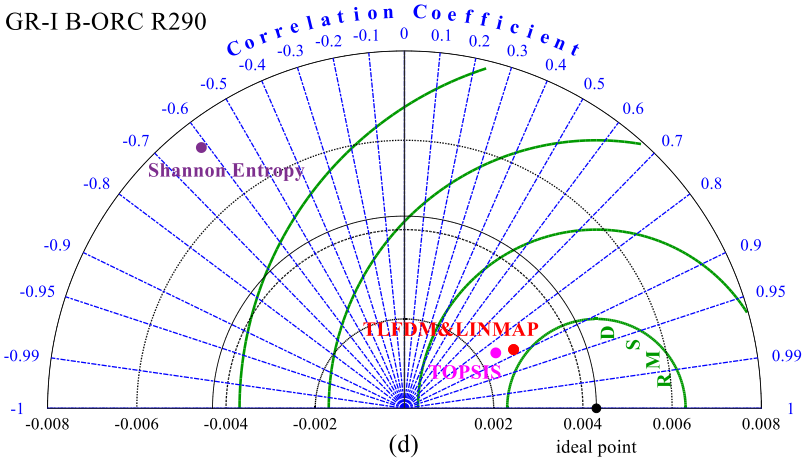
GR-I B-ORC R290
Correlation Coefficient
Shannon Entropy
TLFDM&LINMAP
TOPSIS
RMSD
ideal point
(d)

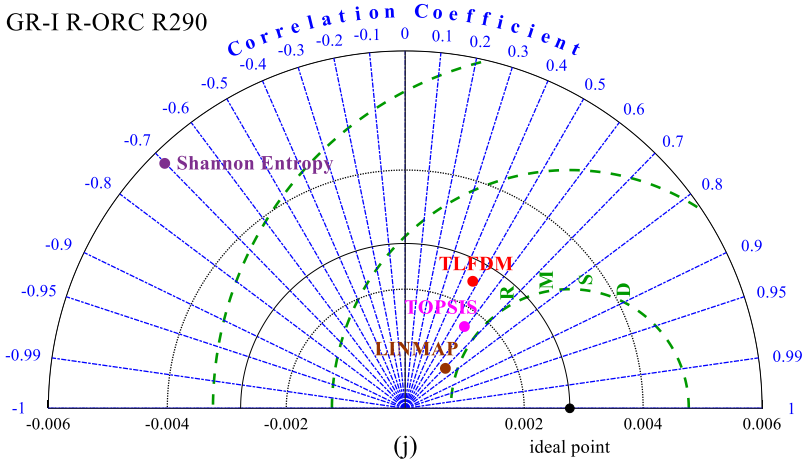
GR-I R-ORC R290
Correlation Coefficient
Shannon Entropy
TLFDM
TOPSIS
LINMAP
RMSD
ideal point
(j)

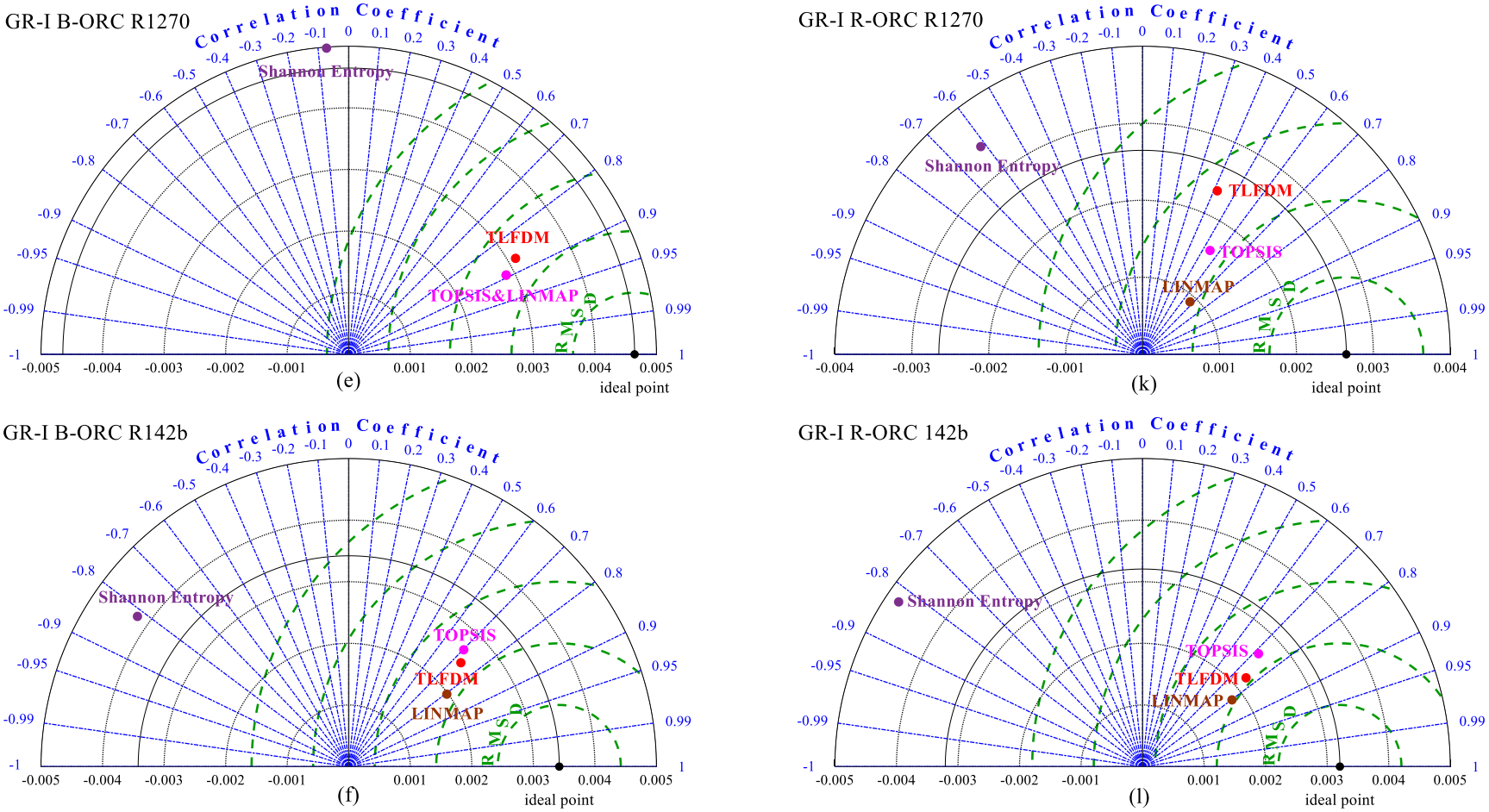

Fig. 9. Taylor diagram for measuring four decision-making points in GR-I.

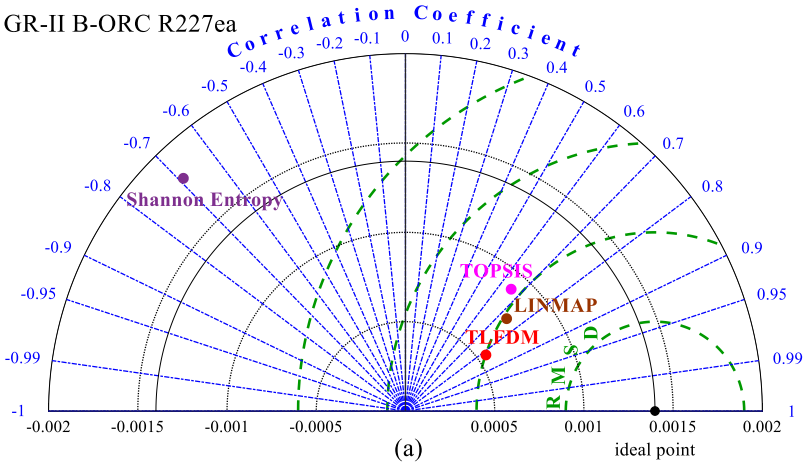
GR-II B-ORC R227ea
Correlation Coefficient
Shannon Entropy
TOPSIS
LINMAP
TLFDM
RMSD
ideal point
(a)

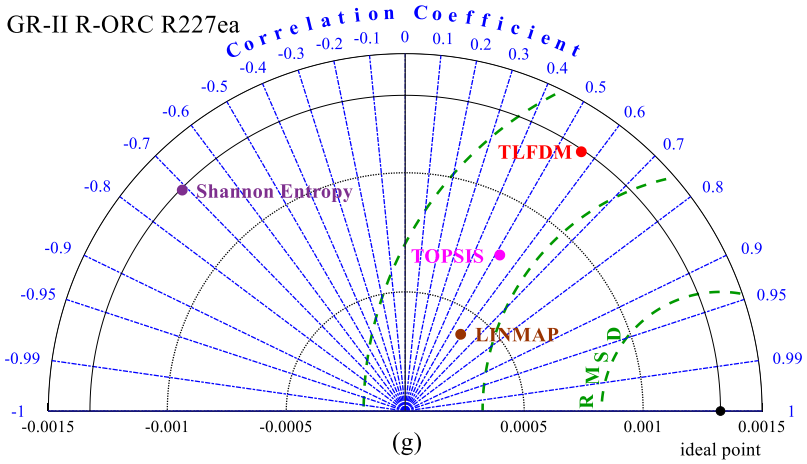
GR-II R-ORC R227ea
Correlation Coefficient
TLFDM
Shannon Entropy
TOPSIS
LINMAP
RMSD
ideal point
(g)

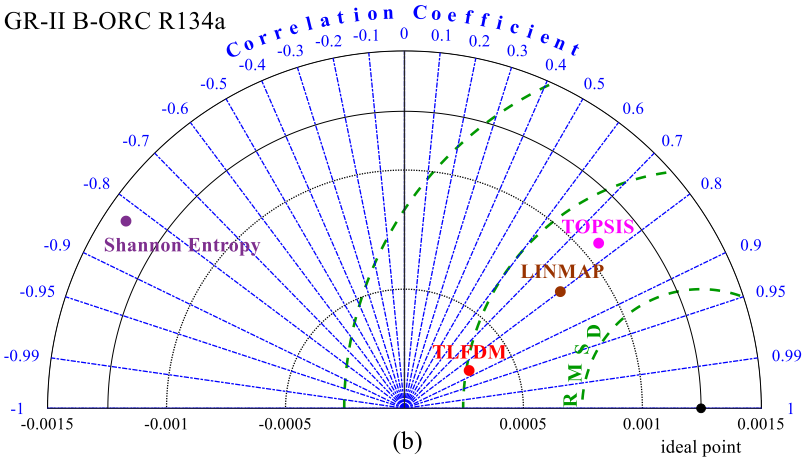
GR-II B-ORC R134a
Correlation Coefficient
Shannon Entropy
TOPSIS
LINMAP
TLFDM
RMSD
ideal point
(b)

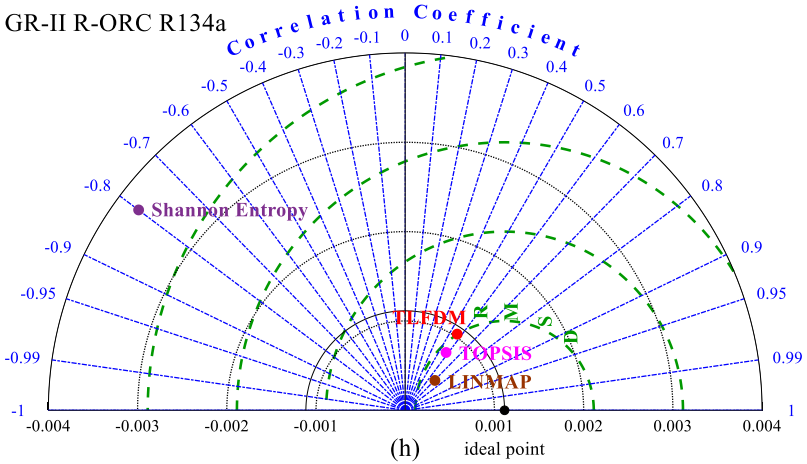
GR-II R-ORC R134a
Correlation Coefficient
Shannon Entropy
TLFDM
TOPSIS
LINMAP
RMSD
ideal point
(h)

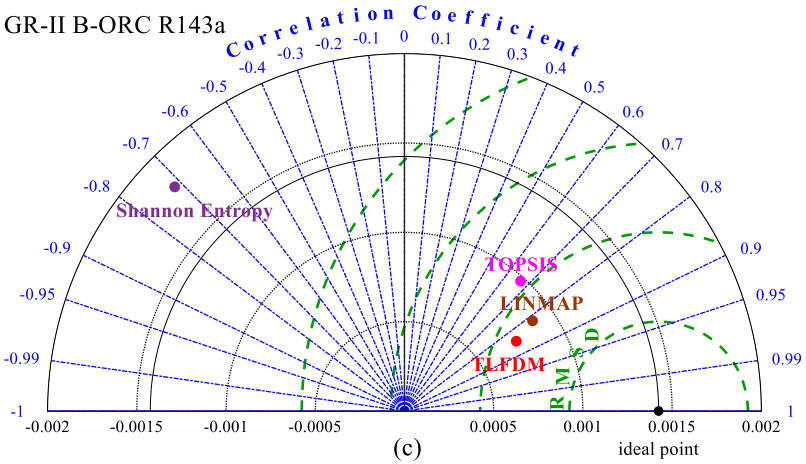
GR-II B-ORC R143a
Correlation Coefficient
Shannon Entropy
TOPSIS
LINMAP
TLFDM
RMSD
ideal point
(c)

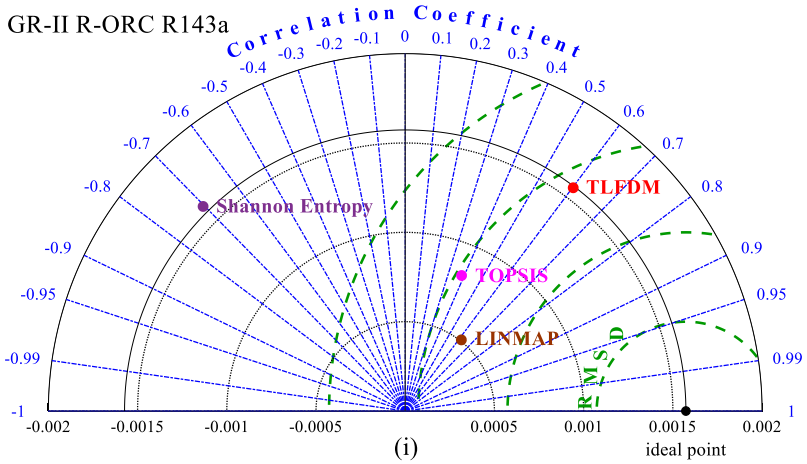
GR-II R-ORC R143a
Correlation Coefficient
TLFDM
Shannon Entropy
TOPSIS
LINMAP
RMSD
ideal point
(i)

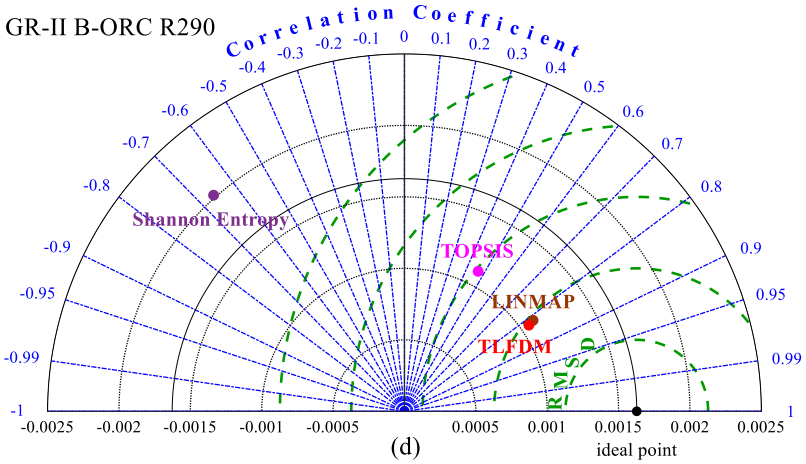
GR-II B-ORC R290
Correlation Coefficient
Shannon Entropy
TOPSIS
LINMAP
TLFDM
RMSD
ideal point
(d)

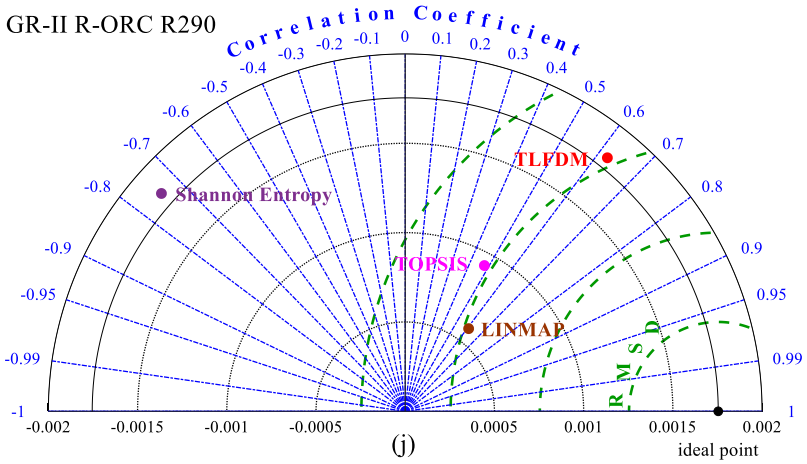
GR-II R-ORC R290
Correlation Coefficient
TLFDM
Shannon Entropy
TOPSIS
LINMAP
RMSD
ideal point
(j)

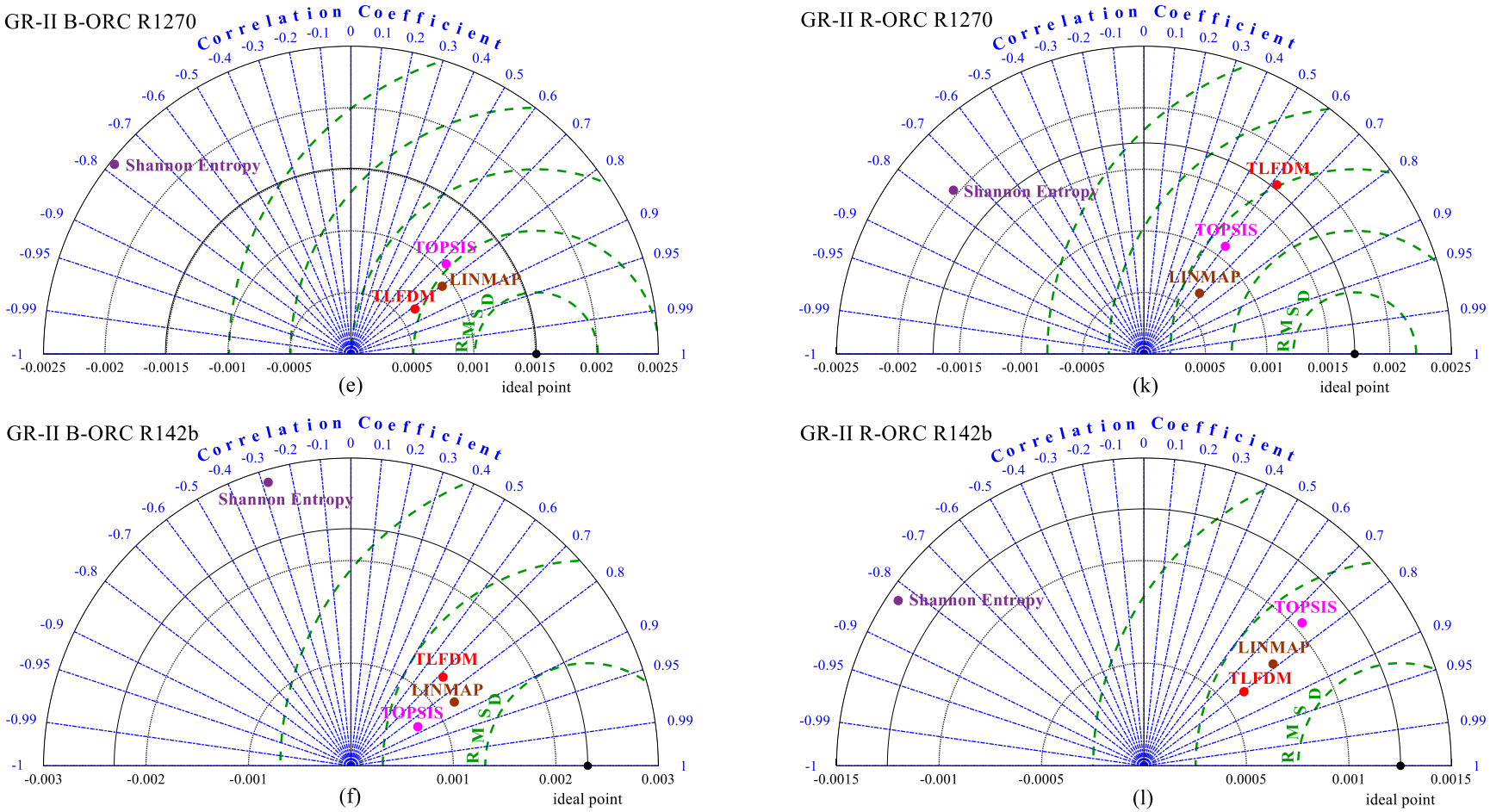

Fig. 10. Taylor diagram for measuring four decision-making points in GR-II.

Figs. 9 and 10 demonstrate the scatter distribution of four decision points in the Taylor diagram. It can be seen the root-mean-square difference (R_{rmsd}), correlation coefficient (C_{coef}) and standard deviation (S_{std}) are indicated by the green dashed arc, blue dotted line and black arc. E.g., the R_{rmsd}, C_{coef} and S_{srd} of LINMAP point for R227ea in the GR-I B-ORC system are 0.0032, 0.8491 and 0.0019, respectively. And the values for the ideal point are 0, 1 and 0.0047. The ideal point in the Taylor diagram is identified with maximal P_{net}, η_t, η_t and S_{IR} as well as minimal A_{PR}, S_P, $Cost_{2019}$, E_{PC} and D_{PP}, which is different from what has been explained in the Pareto optimal frontier. These decision-making points are judged by the rules of lower R_{rmsd} and higher C_{coef}, which is preferred selected with the closest distance from the ideal point. It can be noticed that the Shannon Entropy point is always far away from the ideal point, indicating that the single objective optimal result (maximum net output power point) shouldn't be chosen for the optimized working condition. Moreover, two decision-making points may coincide, such as TLFDM&LINMAP points for R290 in GR-I B-ORC system.

As shown in Figs. 9 and 10, the R_{rmsd} of Shannon Entropy, LINMAP, TOPSIS and TLFDM points for R227ea in GR-I B-ORC system are 0.00973, 0.00325, 0.00354 and 0.00335 respectively, and the C_{coef} are -0.53482, 0.84912, 0.75769 and 0.81213, respectively. As a result, the LINMAP is determined as the final optimal Pareto solution for having the minimum R_{rmsd} and maximum C_{coef}. Similarly, the R_{rmsd} and C_{coef} for the four decision-making points of R227ea in GR-II B-ORC system are 0.00294, 0.00097, 0.00105, 0.00099 and -0.69090, 0.73897, 0.65588, 0.82070, respectively. The R_{rmsd} of TLFDM and LINMAP points are very close, but the C_{coef} of the former is much higher than the latter. Therefore, the TLFDM point is finally chosen. The detailed value for each working fluid of the Taylor diagram in GR-I and GR-II are summarized in the appendix.

A further insight of the binary objectives optimization results are displayed in Tables 6, 7, 8 and 9. It should be noticed that the condensation temperature (T_{cond}) and condenser pinch point temperature ($T_{pinch\text{-}c}$) are centralized around 305K and 10K, which are the minimum and maximum value of their iterative range. Lower T_{cond} is beneficial for the two-phase working fluid condensation as it increases the heat transfer coefficient and reduces the condenser's area and the total cost [42]. Higher $T_{pinch\text{-}c}$ is helpful to increase heat transfer rate and decrease A_{PR}. Nevertheless, the evaporator pinch point temperature ($T_{pinch\text{-}e}$) is dispersed between 7 and 10K, demonstrating that not the higher $T_{pinch\text{-}e}$ the better performance. For the turbine inlet temperature (T_4), it tends to get close to its upper limit to acquire higher P_{net}. Besides that, it also demonstrates R-ORC decreases the evaporation pressure (P_4) and $T_{pinch\text{-}e}$ compared to the B-ORC system, and the final Pareto set point appears frequently at LINMAP and TLFDM points.

Table 6 Pareto-optimal working conditions in GR-I.

Working Fluid	P_4/MPa	T_4/K	T_{cond}/K	$T_{pinch\text{-}e}$/K	$T_{pinch\text{-}c}$/K	Pareto set point
B-ORC R227ea	6.45	438.24	305.00	9.99	10.00	LINMAP
R-ORC R227ea	5.48	440.69	305.00	7.32	10.00	TLFDM
B-ORC R134a	8.00	444.44	305.00	10.00	10.00	LINMAP
R-ORC R134a	6.92	444.92	305.01	8.29	10.00	LINMAP
B-ORC R143a	9.35	445.00	305.00	9.25	10.00	LINMAP
R-ORC R143a	8.09	445.00	305.00	7.68	10.00	LINMAP
B-ORC R290	7.88	445.00	305.00	9.99	9.99	TLFDM&LINMAP
R-ORC R290	7.14	445.00	305.00	7.90	9.99	LINMAP
B-ORC R1270	8.54	444.71	305.00	10.00	10.00	TOPSIS&LINMAP
R-ORC R1270	7.62	445.00	305.00	8.10	10.00	LINMAP
B-ORC R142b	4.90	444.88	305.00	9.81	10.00	LINMAP
R-ORC R142b	4.66	445.00	305.00	8.94	10.00	LINMAP

Table 7 Pareto-optimal working conditions in GR-II.

Working Fluid	P_4/MPa	T_4/K	T_{cond}/K	$T_{pinch\text{-}e}$/K	$T_{pinch\text{-}c}$/K	Pareto set point
B-ORC R227ea	8.78	470.00	305.00	8.04	10.00	TLFDM
R-ORC R227ea	6.98	470.00	305.00	7.38	10.00	LINMAP
B-ORC R134a	7.59	440.00	305.00	8.63	10.00	LINMAP
R-ORC R134a	6.37	440.00	305.00	7.77	10.00	LINMAP
B-ORC R143a	12.92	485.00	305.00	8.37	10.00	TLFDM
R-ORC R143a	10.27	485.00	305.00	7.85	10.00	LINMAP
B-ORC R290	11.16	485.00	305.00	9.52	10.00	TLFDM
R-ORC R290	9.32	485.00	305.00	8.00	10.00	LINMAP
B-ORC R1270	12.00	485.00	305.00	9.33	10.00	LINMAP
R-ORC R1270	9.76	485.00	305.00	7.97	10.00	LINMAP
B-ORC R142b	5.49	454.50	305.00	9.94	10.00	LINMAP
R-ORC R142b	4.96	455.00	305.00	8.45	10.00	LINMAP

Table 8 Pareto-optimal results in GR-I.

Working Fluid	P_{net}/kW	η_t/%	η_e/%	A_{PR}(m^2/kW)	S_P/m	$Cost_{2019}$(10^5\$)	E_{PC}(\$/(kW·h))	D_{PP}/Year	S_{IR}	Pareto set point
B-ORC R227ea	1199.09	10.97	40.57	0.241	0.071	29.71	0.035	3.600	3.457	LINMAP
R-ORC R227ea	1292.20	14.71	48.41	0.222	0.072	32.37	0.035	3.646	3.419	TLFDM
B-ORC R134a	1380.13	12.70	46.77	0.221	0.066	30.79	0.031	3.193	3.839	LINMAP
R-ORC R134a	1408.93	14.89	50.64	0.215	0.067	33.15	0.033	3.392	3.641	LINMAP
B-ORC R143a	1185.50	11.07	40.37	0.232	0.053	30.91	0.036	3.818	3.285	LINMAP
R-ORC R143a	1245.18	13.85	46.02	0.218	0.055	33.18	0.037	3.916	3.215	LINMAP
B-ORC R290	1331.52	12.33	45.22	0.215	0.072	30.66	0.032	3.311	3.719	TLFDM&LINMAP
R-ORC R290	1356.49	14.77	49.54	0.207	0.073	33.05	0.034	3.531	3.516	LINMAP
B-ORC R1270	1322.05	12.30	44.97	0.205	0.066	30.61	0.032	3.330	3.700	TOPSIS&LINMAP
R-ORC R1270	1343.61	14.36	48.59	0.200	0.067	32.88	0.034	3.549	3.500	LINMAP
B-ORC R142b	1573.41	14.42	53.25	0.210	0.091	30.48	0.027	2.725	4.422	LINMAP
R-ORC R142b	1570.72	16.21	55.79	0.209	0.091	33.26	0.029	3.010	4.045	LINMAP

Table 9 Pareto-optimal results in GR-II.

Working Fluid	P_{net}/kW	η_t/%	η_e/%	A_{PR}(m^2/kW)	S_P/m	$Cost_{2019}$(10^5\$)	E_{PC}(\$/(kW·h))	D_{PP}/Year	S_{IR}	Pareto set point
B-ORC R227ea	1772.89	11.66	34.83	0.163	0.070	32.91	0.026	2.599	4.614	TLFDM
R-ORC R227ea	2114.75	16.61	44.89	0.138	0.071	35.87	0.024	2.353	5.050	LINMAP
B-ORC R134a	1906.52	12.52	37.44	0.145	0.066	31.97	0.023	2.324	5.107	LINMAP
R-ORC R134a	2053.69	14.58	41.41	0.142	0.068	34.86	0.024	2.355	5.046	LINMAP
B-ORC R143a	1851.42	12.43	36.58	0.151	0.052	35.56	0.027	2.699	4.460	TLFDM
R-ORC R143a	2124.32	16.67	45.05	0.134	0.054	37.64	0.025	2.468	4.835	LINMAP
B-ORC R290	2048.57	13.69	40.42	0.139	0.070	34.71	0.024	2.350	5.056	TLFDM
R-ORC R290	2267.51	17.65	47.87	0.126	0.072	37.03	0.023	2.257	5.245	LINMAP
B-ORC R1270	2067.73	13.86	40.83	0.132	0.065	35.10	0.024	2.355	5.046	LINMAP
R-ORC R1270	2257.30	17.26	47.19	0.122	0.067	36.98	0.023	2.265	5.229	LINMAP
B-ORC R142b	2255.32	14.79	44.28	0.130	0.090	31.67	0.020	1.916	6.101	LINMAP
R-ORC R142b	2376.73	16.94	48.01	0.128	0.091	34.86	0.020	2.008	5.839	LINMAP

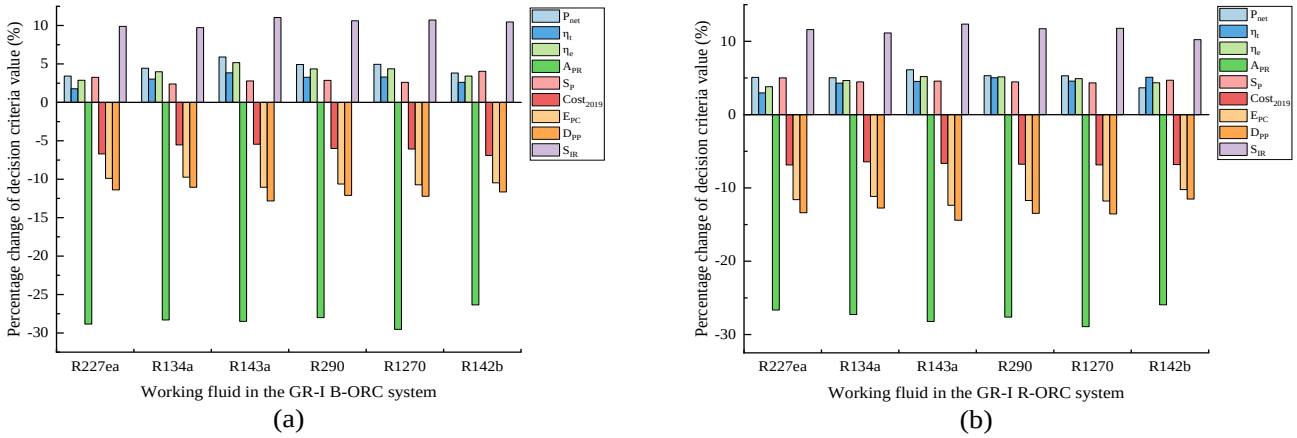

(a) (b)

Fig. 11. Percentage change of decision criteria value after NSGA-II optimization in GR-I (%).

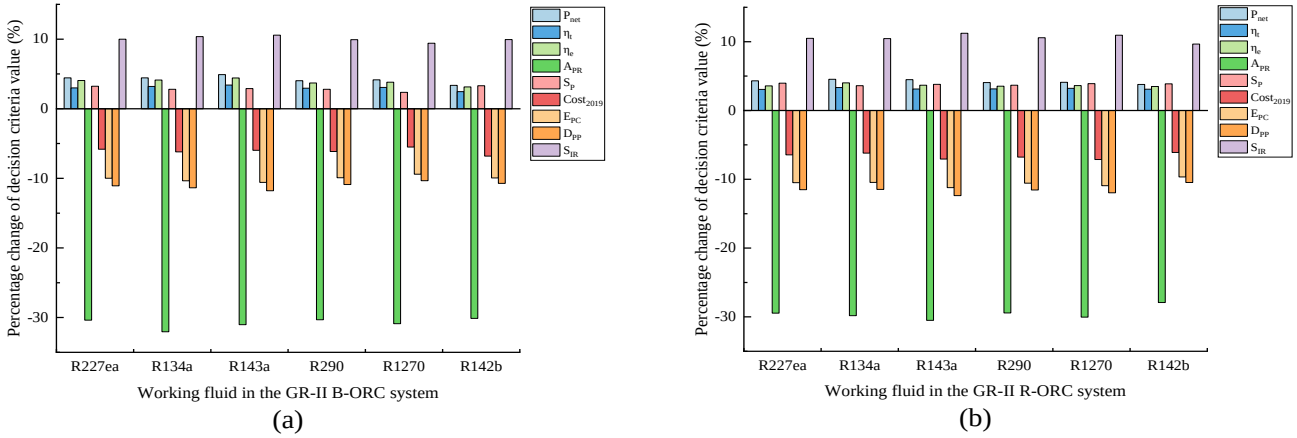

(a) (b)

Fig. 12. Percentage change of decision criteria value after NSGA-II optimization in GR-II (%).

Tables 8 and 9 list the Pareto-optimal results in GR-I and GR-II which refer to the thermodynamic and techno-economic criteria. It is shown that R142b performs best in both geothermal reservoirs while R143a manifests undesirable performance among the six working fluids. Furthermore, the values of P_{net}, η_t and S_{IR} in GR-II are generally higher than those in GR-I. But the η_e displays an opposite trend for that the exergy loss has increased in GR-II, and this variation is consistent with the published literature [26], showing that the exergy of high temperature geothermal reservoir was not fully utilized compared to the lower temperature one. The A_{PR}, S_P, E_{PC} and D_{PP} of GR-II are less than those of GR-I, indicating that higher heat source temperature working condition is favorable for geothermal energy exploitation. Moreover, it can be seen that R-ORC has strengthened the system thermodynamic performance but weakened the techno-economic performance in GR-I. The advantageous variation is that P_{net}, η_t, η_e increases and A_{PR} decreases. But for R142b, the P_{net} of R-ORC is slightly lower than that of B-ORC because the mass flow rate of working fluid decreases. Meanwhile, the adverse effect lies in that $Cost_{2019}$, E_{PC}, D_{PP} exhibit a trend of increment and a reduction in S_{IR} as well. On the contrary, R-ORC has not only improved the system's thermodynamic performance but also the techno-economic performance in most cases of GR-II, indicating that the R-ORC is more suitable for higher temperature working conditions.

Comparing the percentage change value of evaluation criteria for Pareto-optimal results with non-optimized solutions [26] tabulated in Figs. 11 and 12, it is found that the whole system performance has been improved a lot after the NSGA-II optimization. The positive alteration implies an increase while the negative one represents a decrease. Specifically, R143a exhibits the largest growth rate in P_{net}, E_{PC}, D_{PP} and S_{IR}. The most obvious change is A_{PR} which decreases averagely more than 27.0% and 30.0% in GR-I and GR-II. And it directly accounts for a decline in the total cost. The adverse effect of the optimization is that S_P shows an increment to imply the compactness of the turbine has weakened.

6 Conclusion

In this paper, a Four-Hierarchy method is developed to achieve effective and practical design and optimization along with decision-making for ORC systems. The optimal operating parameters for the medium (GR-I) and high (GR-II) temperature geothermal ORC systems have been revealed based on the NSGA-II algorithm. Four decision-making methods are applied to determine four Pareto-optimal solutions. Taylor diagram is used to find the final Pareto-optimal solution. The main conclusions are summarized as follows:

1. Compared with the basic trans-critical ORC system, the recuperative trans-critical ORC is more effective to acquire better thermodynamic and techno-economic performance under high temperature geothermal working conditions.

2. Modified LINMAP and TLFDM points are selected more frequently as the final Pareto-optimal solutions through the Taylor diagram. Shannon Entropy is not applicable for decision-making alone.

3. The overall performance of the geothermal ORC system has been improved after optimization and the most significant alteration is heat transfer area per net output power, which decreased averagely by 27.0% and 30.0% in the medium and high temperature geothermal reservoirs, respectively.

4. The condensation temperature and condenser pinch point temperature tend to be 305K and 10K respectively, while evaporator pinch point temperature ranges from 7K to 10K. Moreover, R142b consistently performs the best to obtain the highest net output power and largest saving to investment ratio.

According to the proposed methods, the robust mathematical model, optimization and decision-making hierarchy have been constructed, aiming at implementing the comprehensive quantitative evaluation of the performance for various ORC power plants, and realizing an intuitive comparison of the advantages and disadvantages of different scenarios. By using this systematic approach, it is possible to save time while effectively converting heat sources. And it can provide certain scientific guidance to the design of sustainable energy conversion systems.

Acknowledgement

Author Guopeng Yu acknowledges the support by the Funding of Hundred Talents Program of Sun Yat-sen University. Author Qinggang Wang would like to show gratitude to Jiyue Wang and Muchuan Zhou for the computational support.

Appendix Taylor diagram evaluation results

B-ORC R227ea	C_{coef}	R_{rmsd}	S_{std}
Ideal point	1	0	0.004733
Shannon Entropy	-0.534821	0.009736	0.006346
LINMAP	0.849127	0.003259	0.001928
TOPSIS	0.757694	0.003548	0.001840
TLFDM	0.812137	0.003351	0.001946

R-ORC R227ea	C_{coef}	R_{rmsd}	S_{std}
Ideal point	1	0	0.002614
Shannon Entropy	-0.684120	0.005083	0.002923
LINMAP	0.643227	0.002132	0.000947
TOPSIS	0.562375	0.002162	0.001491
TLFDM	0.644382	0.002092	0.001068

B-ORC R134a	C_{coef}	R_{rmsd}	S_{std}
Ideal point	1	0	0.004778
Shannon Entropy	-0.286504	0.007533	0.004614
LINMAP	0.900246	0.002980	0.002168
TOPSIS	0.878064	0.003426	0.001644
TLFDM	0.690480	0.003523	0.002619

R-ORC R134a	C_{coef}	R_{rmsd}	S_{std}
Ideal point	1	0	0.002697
Shannon Entropy	-0.734961	0.008343	0.006158
LINMAP	0.728229	0.002051	0.001076
TOPSIS	0.633751	0.002086	0.001746
TLFDM	0.754888	0.002258	0.000631

B-ORC R143a	C_{coef}	R_{rmsd}	S_{std}
Ideal point	1	0	0.002435
Shannon Entropy	-0.600408	0.005068	0.003217
LINMAP	0.808130	0.001646	0.001161
TOPSIS	0.727526	0.001736	0.001299
TLFDM	0.834191	0.001786	0.000854

R-ORC R143a	C_{coef}	R_{rmsd}	S_{std}
Ideal point	1	0	0.002538
Shannon Entropy	-0.730624	0.005749	0.003627
LINMAP	0.692142	0.001953	0.001079
TOPSIS	0.594534	0.002057	0.001763
TLFDM	0.456714	0.002696	0.002633

B-ORC R290	C_{coef}	R_{rmsd}	S_{std}
Ideal point	1	0	0.004303
Shannon Entropy	-0.615012	0.010607	0.007403
LINMAP	0.880836	0.002275	0.002778
TOPSIS	0.855172	0.002574	0.002394
TLFDM	0.880836	0.002275	0.002778

R-ORC R290	C_{coef}	R_{rmsd}	S_{std}
Ideal point	1	0	0.002767
Shannon Entropy	-0.701124	0.007956	0.005767
LINMAP	0.709543	0.002197	0.000952
TOPSIS	0.586735	0.002242	0.001696
TLFDM	0.469931	0.002685	0.002416

B-ORC R1270	C_{coef}	R_{rmsd}	S_{std}
Ideal point	1	0	0.004645
Shannon Entropy	-0.072377	0.007054	0.004982
LINMAP	0.893461	0.002451	0.002864
TOPSIS	0.893461	0.002451	0.002864
TLFDM	0.867112	0.002483	0.003126

R-ORC R1270	C_{coef}	R_{rmsd}	S_{std}
Ideal point	1	0	0.002649
Shannon Entropy	-0.615030	0.005465	0.003421
LINMAP	0.670954	0.002143	0.000919
TOPSIS	0.545323	0.002226	0.001608
TLFDM	0.415939	0.002706	0.002334

B-ORC R142b	C_{coef}	R_{rmsd}	S_{std}
Ideal point	1	0	0.003422
Shannon Entropy	-0.815393	0.007275	0.004210
LINMAP	0.804884	0.002173	0.001981
TOPSIS	0.702114	0.002450	0.002662
TLFDM	0.734115	0.002324	0.002482

R-ORC R142b	C_{coef}	R_{rmsd}	S_{std}
Ideal point	1	0	0.003206
Shannon Entropy	-0.829180	0.007652	0.004780
LINMAP	0.801726	0.002061	0.001811
TOPSIS	0.716929	0.002259	0.002628
TLFDM	0.759223	0.002098	0.002214

Fig. 13. Correlation coefficient, R_{rmsd} and standard deviation of Taylor diagram in GR-I.

B-ORC R227ea	C_{coef}	R_{rmsd}	S_{std}
Ideal point	1	0	0.001398
Shannon Entropy	-0.690901	0.002947	0.001802
LINMAP	0.738970	0.000979	0.000767
TOPSIS	0.655885	0.001056	0.000903
TLFDM	0.820702	0.000998	0.000549

R-ORC R227ea	C_{coef}	R_{rmsd}	S_{std}
Ideal point	1	0	0.001325
Shannon Entropy	-0.710830	0.002445	0.001319
LINMAP	0.586295	0.001139	0.000398
TOPSIS	0.518924	0.001135	0.000766
TLFDM	0.562378	0.001236	0.001316

B-ORC R134a	C_{coef}	R_{rmsd}	S_{std}
Ideal point	1	0	0.001247
Shannon Entropy	-0.830273	0.002542	0.001410
LINMAP	0.800907	0.000768	0.000818
TOPSIS	0.762169	0.000816	0.001071
TLFDM	0.863616	0.000988	0.000315

R-ORC R134a	C_{coef}	R_{rmsd}	S_{std}
Ideal point	1	0	0.001113
Shannon Entropy	-0.799788	0.004675	0.003736
LINMAP	0.705058	0.000849	0.000472
TOPSIS	0.577341	0.000921	0.000793
TLFDM	0.564113	0.001004	0.001033

B-ORC R143a	C_{coef}	R_{rmsd}	S_{std}
Ideal point	1	0	0.001425
Shannon Entropy	-0.716240	0.002988	0.001798
LINMAP	0.817918	0.000869	0.000878
TOPSIS	0.667084	0.001062	0.000976
TLFDM	0.848776	0.000888	0.000739

R-ORC R143a	C_{coef}	R_{rmsd}	S_{std}
Ideal point	1	0	0.001573
Shannon Entropy	-0.703324	0.002938	0.001611
LINMAP	0.619857	0.001320	0.000507
TOPSIS	0.384475	0.001468	0.000822
TLFDM	0.601799	0.001400	0.001564

B-ORC R290	C_{coef}	R_{rmsd}	S_{std}
Ideal point	1	0	0.001627
Shannon Entropy	-0.662569	0.003328	0.002018
LINMAP	0.816841	0.000966	0.001103
TOPSIS	0.466252	0.001481	0.001107
TLFDM	0.822390	0.000967	0.001060

R-ORC R290	C_{coef}	R_{rmsd}	S_{std}
Ideal point	1	0	0.001754
Shannon Entropy	-0.746163	0.003350	0.001831
LINMAP	0.609107	0.001473	0.000583
TOPSIS	0.477776	0.001544	0.000929
TLFDM	0.623989	0.001549	0.001816

B-ORC R1270	C_{coef}	R_{rmsd}	S_{std}
Ideal point	1	0	0.001509
Shannon Entropy	-0.780595	0.003762	0.002464
LINMAP	0.803757	0.000943	0.000924
TOPSIS	0.727080	0.001036	0.001065
TLFDM	0.818731	0.001053	0.000636

R-ORC R1270	C_{coef}	R_{rmsd}	S_{std}
Ideal point	1	0	0.001714
Shannon Entropy	-0.758867	0.003524	0.002042
LINMAP	0.675696	0.001355	0.000669
TOPSIS	0.603532	0.001368	0.001096
TLFDM	0.618217	0.001513	0.001748

B-ORC R142b	C_{coef}	R_{rmsd}	S_{std}
Ideal point	1	0	0.002311
Shannon Entropy	-0.280534	0.004167	0.002879
LINMAP	0.851529	0.001443	0.001185
TOPSIS	0.863982	0.001701	0.000756
TLFDM	0.720759	0.001656	0.001247

R-ORC R142b	C_{coef}	R_{rmsd}	S_{std}
Ideal point	1	0	0.001252
Shannon Entropy	-0.830240	0.002580	0.001445
LINMAP	0.785652	0.000796	0.000802
TOPSIS	0.742176	0.000846	0.001039
TLFDM	0.804061	0.000845	0.000607

Fig. 14. Correlation coefficient, R_{rmsd} and standard deviation of Taylor diagram in GR-II.

Reference

[1] Liang Y, Shu G, Wei H, Zhang W. Effect of oxygen enriched combustion and water–diesel emulsion. Energy Convers Manage 2013;73:69-77. https://doi.org/10.1016/j.enconman.2013.04.023.

[2] Yang F, Dong X, Zhang H, Wang Z, Yang K, Zhang J, et al. Performance analysis of waste heat recovery with a dual loop organic Rankine cycle (ORC) system for diesel engine under various operating conditions. Energy Convers Manage 2014;80:243-255. https://doi.org/10.1016/j.enconman.2014.01.036.

[3] Shu G, Shi L, Tian H, Li X, Huang G, Chang L. An improved CO2-based transcritical Rankine cycle (CTRC) used for engine waste heat recovery. Appl Energ 2016;176:171-182. https://doi.org/10.1016/j.apenergy.2016.05.053.

[4] Li X, Shu G, Tian H, Shi L, Huang G, Chen T, et al. Preliminary tests on dynamic characteristics of a CO2 transcritical power cycle using an expansion valve in engine waste heat recovery. Energy 2017;140:696-707. https://doi.org/10.1016/j.energy.2017.09.022.

[5] Shi L, Shu G, Tian H, Deng S. A review of modified Organic Rankine cycles (ORCs) for internal combustion engine waste heat recovery (ICE-WHR). Renew Sust Energ Rev 2018;92:95-110. https://doi.org/10.1016/j.rser.2018.04.023.

[6] Moloney F, Almatrafi E, Goswami DY. Working fluid parametric analysis for recuperative supercritical organic Rankine cycles for medium geothermal reservoir temperatures. Renew Energ 2020;147:2874-2881. https://doi.org/10.1016/j.renene.2018.09.003.

[7] Song J, Li X, Ren X, Tian H, Shu G, Gu C, et al. Thermodynamic and economic investigations of transcritical CO2-cycle systems with integrated radial-inflow turbine performance predictions. Appl Therm Eng 2020;165. https://doi.org/10.1016/j.applthermaleng.2019.114604.

[8] Çetin G, Keçebaş A. Optimization of thermodynamic performance with simulated annealing algorithm: A geothermal power plant. Renew Energ 2021;172:968-982. https://doi.org/10.1016/j.renene.2021.03.101.

[9] Kolahi M-R, Amidpour M, Yari M. Multi-objective metaheuristic optimization of combined flash-binary geothermal and humidification dehumidification desalination systems. Desalination 2020;490:114456. https://doi.org/10.1016/j.desal.2020.114456.

[10] Pratama F, Reyseliani N, Syauqi A, Daud Y, Purwanto WW, Wulan PPDK, et al. Thermoeconomic assessment and optimization of wells to flash–binary cycle using pure R601 and zeotropic mixtures in the Sibayak geothermal field. Geothermics 2020;85:101778. https://doi.org/10.1016/j.geothermics.2019.101778.

[11] Van Erdeweghe S, Van Bael J, Laenen B, D'haeseleer W. Design and off-design optimization procedure for low-temperature geothermal organic Rankine cycles. Appl Energ 2019;242:716-731. https://doi.org/https://doi.org/10.1016/j.apenergy.2019.03.142.

[12] Karimi S, Mansouri S. A comparative profitability study of geothermal electricity production in developed and developing countries: Exergoeconomic analysis and optimization of different ORC configurations. Renew Energ 2018;115:600-619. https://doi.org/10.1016/j.renene.2017.08.098.
[13] Liu X, Wei M, Yang L, Wang X. Thermo-economic analysis and optimization selection of ORC system configurations for low temperature binary-cycle geothermal plant. Appl Therm Eng 2017;125:153-164. https://doi.org/10.1016/j.applthermaleng.2017.07.016.
[14] Arslan O, Yetik O. ANN based optimization of supercritical ORC-Binary geothermal power plant: Simav case study. Appl Therm Eng 2011;31:3922-3928. https://doi.org/10.1016/j.applthermaleng.2011.07.041.
[15] Alimonti C, Conti P, Soldo E. Producing geothermal energy with a deep borehole heat exchanger: Exergy optimization of different applications and preliminary design criteria. Energy 2021;220:119679. https://doi.org/10.1016/j.energy.2020.119679.
[16] Cao Y, Dhahad HA, Togun H, Hussen HM, Anqi AE, Farouk N, et al. Thermodynamic and economic assessments and multi-criteria optimization of a novel poly-generation plant using geothermal energy and multi heat recovery technique. Int J Hydrogen Energ 2021;46:27851-27873. https://doi.org/https://doi.org/10.1016/j.ijhydene.2021.06.063.
[17] Musharavati F, Khanmohammadi S, Pakseresht AH, Khanmohammadi S. Enhancing the performance of an integrated CCHP system including ORC, Kalina, and refrigeration cycles through employing TEG: 3E analysis and multi-criteria optimization. Geothermics 2021;89:101973. https://doi.org/10.1016/j.geothermics.2020.101973.
[18] Aliahmadi M, Moosavi A, Sadrhosseini H. Multi-objective optimization of regenerative ORC system integrated with thermoelectric generators for low-temperature waste heat recovery. Energy Rep 2021;7:300-313. https://doi.org/10.1016/j.egyr.2020.12.035.
[19] Lu P, Luo X, Wang J, Chen J, Liang Y, Yang Z, et al. Thermo-economic design, optimization, and evaluation of a novel zeotropic ORC with mixture composition adjustment during operation. Energy Convers Manage 2021;230:113771. https://doi.org/10.1016/j.enconman.2020.113771.
[20] Nasruddin N, Dwi Saputra I, Mentari T, Bardow A, Marcelina O, Berlin S. Exergy, exergoeconomic, and exergoenvironmental optimization of the geothermal binary cycle power plant at Ampallas, West Sulawesi, Indonesia. Therm Sci Eng Prog 2020;19:100625. https://doi.org/10.1016/j.tsep.2020.100625.
[21] Wang L, Li H, Bu X. Multi-objective optimization of Binary Flashing Cycle (BFC) driven by geothermal energy. Appl Therm Eng 2020;166:114693. https://doi.org/10.1016/j.applthermaleng.2019.114693.

[22] Imran M, Usman M, Park B-S, Kim H-J, Lee D-H. Multi-objective optimization of evaporator of organic Rankine cycle (ORC) for low temperature geothermal heat source. Appl Therm Eng 2015;80:1-9. https://doi.org/10.1016/j.applthermaleng.2015.01.034.
[23] Liu X, Zhang Y, Shen J. System performance optimization of ORC-based geo-plant with R245fa under different geothermal water inlet temperatures. Geothermics 2017;66:134-142. https://doi.org/10.1016/j.geothermics.2016.12.004.
[24] Shokati N, Ranjbar F, Yari M. Exergoeconomic analysis and optimization of basic, dual-pressure and dual-fluid ORCs and Kalina geothermal power plants: A comparative study. Renew Energ 2015;83:527-542. https://doi.org/https://doi.org/10.1016/j.renene.2015.04.069.
[25] Madhawa Hettiarachchi HD, Golubovic M, Worek WM, Ikegami Y. Optimum design criteria for an Organic Rankine cycle using low-temperature geothermal heat sources. Energy 2007;32:1698-1706. https://doi.org/10.1016/j.energy.2007.01.005.
[26] Zhang N, Wang Q, Yu Z, Yu G. A non-structural fuzzy decision method developed for organic Rankine cycles used in liquid-dominated geothermal fields of medium/high temperature. Energy Convers Manage 2021;231:113861. https://doi.org/10.1016/j.enconman.2021.113861.
[27] Imran M, Usman M, Park B-S, Yang Y. Comparative assessment of Organic Rankine Cycle integration for low temperature geothermal heat source applications. Energy 2016;102:473-490. https://doi.org/10.1016/j.energy.2016.02.119.
[28] Martin H. A theoretical approach to predict the performance of chevron-type plate heat exchangers. Chem Eng Process 1996;35:301-310. https://doi.org/10.1016/0255-2701(95)04129-x.
[29] Wang Z-Z, Zhao Z-N. Analysis of Performance of Steam Condensation Heat Transfer and Pressure Drop in Plate Condensers. Heat Transfer Eng 1993;14:32-41. https://doi.org/10.1080/01457639308939809.
[30] Pioro IL, Khartabil HF, Duffey RB. Heat transfer to supercritical fluids flowing in channels—empirical correlations (survey). Nucl Eng Des 2004;230:69-91. https://doi.org/10.1016/j.nucengdes.2003.10.010.
[31] Hu D, Li S, Zheng Y, Wang J, Dai Y. Preliminary design and off-design performance analysis of an Organic Rankine Cycle for geothermal sources. Energy Convers Manage 2015;96:175-187. https://doi.org/10.1016/j.enconman.2015.02.078.
[32] Kuo WS, Lie YM, Hsieh YY, Lin TF. Condensation heat transfer and pressure drop of refrigerant R-410A flow in a vertical plate heat exchanger. Int J Heat Mass Tran 2005;48:5205-5220. https://doi.org/10.1016/j.ijheatmasstransfer.2005.07.023.

[33] Le VL, Feidt M, Kheiri A, Pelloux-Prayer S. Performance optimization of low-temperature power generation by supercritical ORCs (organic Rankine cycles) using low GWP (global warming potential) working fluids. Energy 2014;67:513-526. https://doi.org/10.1016/j.energy.2013.12.027.
[34] Feng Y, Hung T, Zhang Y, Li B, Yang J, Shi Y. Performance comparison of low-grade ORCs (organic Rankine cycles) using R245fa, pentane and their mixtures based on the thermoeconomic multi-objective optimization and decision makings. Energy 2015;93:2018-2029. https://doi.org/10.1016/j.energy.2015.10.065.
[35] Ahmadi MH, Ahmadi MA, Sadatsakkak SA. Thermodynamic analysis and performance optimization of irreversible Carnot refrigerator by using multi-objective evolutionary algorithms (MOEAs). Renew Sust Energ Rev 2015;51:1055-1070. https://doi.org/10.1016/j.rser.2015.07.006.
[36] Şengül Ü, Eren M, Eslamian Shiraz S, Gezder V, Şengül AB. Fuzzy TOPSIS method for ranking renewable energy supply systems in Turkey. Renew Energ 2015;75:617-625. https://doi.org/10.1016/j.renene.2014.10.045.
[37] Boyaghchi FA, Chavoshi M. Monthly assessments of exergetic, economic and environmental criteria and optimization of a solar micro-CCHP based on DORC. Sol Energy 2018;166:351-370. https://doi.org/10.1016/j.solener.2018.03.069.
[38] Habibollahzade A, Houshfar E. Improved performance and environmental indicators of a municipal solid waste fired plant through CO2 recycling: Exergoeconomic assessment and multi-criteria grey wolf optimisation. Energy Convers Manage 2020;225:113451. https://doi.org/10.1016/j.enconman.2020.113451.
[39] Cao Y, Nikafshan Rad H, Hamedi Jamali D, Hashemian N, Ghasemi A. A novel multi-objective spiral optimization algorithm for an innovative solar/biomass-based multi-generation energy system: 3E analyses, and optimization algorithms comparison. Energy Convers Manage 2020;219:112961. https://doi.org/10.1016/j.enconman.2020.112961.
[40] Mehrpooya M, Ashouri M, Mohammadi A. Thermoeconomic analysis and optimization of a regenerative two-stage organic Rankine cycle coupled with liquefied natural gas and solar energy. Energy 2017;126:899-914. https://doi.org/https://doi.org/10.1016/j.energy.2017.03.064.
[41] Zhou G-Y, Wu E, Tu S-T. Optimum selection of compact heat exchangers using non-structural fuzzy decision method. Appl Energ 2014;113:1801-1809. https://doi.org/10.1016/j.apenergy.2013.07.041.
[42] Jankowski M, Borsukiewicz A, Wiśniewski S, Hooman K. Multi-objective analysis of an influence of a geothermal water salinity on optimal operating parameters in low-temperature ORC power plant. Energy 2020;202. https://doi.org/10.1016/j.energy.2020.117666.